

Contents

| | |
|--|-----------|
| List of figures | v |
| List of tables | vi |
| 1 Introduction | 1 |
| 2 Introduction | 2 |
| 2.1 Initial Goal of the Internship | 2 |
| 2.2 Problem | 2 |
| 3 Theory | 3 |
| 3.1 Chemistry | 3 |
| 3.1.1 Oxalic Acid | 3 |
| 3.1.2 Phosphoric Acid | 3 |
| 3.1.3 Aluminum Dissolution Acid | 3 |
| 3.2 Ideal Gas Law | 3 |
| 3.2.1 Boyle–Mariotte Law | 3 |
| 3.3 Hexane | 4 |
| 3.3.1 Saturated Vapor Pressure | 4 |
| 3.3.2 Liquid Density | 4 |
| 3.3.3 Gas Density | 4 |
| 3.4 Laplace–Young equation | 4 |
| 3.5 Kelvin Equation | 4 |
| 3.6 Condensation and evaporation in a cylindrical pore | 5 |
| 3.6.1 Closed pore | 6 |
| 3.6.1.1 Closed straight pore | 6 |
| 3.6.1.2 Closed funneled pore - large end open | 6 |
| 3.6.1.3 Closed funnelled pore - small end open | 6 |
| 3.6.2 Open cylindrical pore | 7 |
| 3.6.2.1 Open straight pore | 7 |
| 3.6.2.2 Open funnelled pore | 7 |
| 3.6.3 Isotherm comparison | 13 |
| 3.7 Snell's Law | 13 |
| 3.8 Fresnel Equations | 14 |
| 3.8.1 Two Interface Transmission | 15 |
| 3.9 Blablabla Näherung | 16 |
| 3.9.1 Transmission of Nanoporous Membranes in Empty and Filled State | 17 |
| 3.9.1.1 Transmission of Empty AAM Membrane | 17 |
| 3.10 Rayleigh Scattering | 18 |
| 3.11 Index Matching | 18 |

| | |
|---|-----------|
| 4 Experimental | 19 |
| 4.1 Alumina Membranes | 19 |
| 4.1.1 Membrane Production | 19 |
| 4.1.1.1 Anodizing | 19 |
| 4.1.1.2 Aluminum Dissolution | 21 |
| 4.1.1.3 Barrier Layer Dissolution | 22 |
| 4.1.2 Membrane Specifications | 22 |
| 4.2 Experimental setup | 23 |
| 4.2.1 Volumetric setup | 23 |
| 4.2.1.1 Cell temperature regulation | 24 |
| 4.2.1.2 Pressure gauges | 24 |
| 4.2.2 Laser transmission setup | 24 |
| 4.2.3 Camera setup | 24 |
| 4.3 Experimental procedure | 24 |
| 4.3.1 Bypass | 25 |
| 4.3.1.1 Changing the membrane | 26 |
| 5 Analysis | 27 |
| 5.1 Computing the isotherms | 27 |
| 5.1.1 Determination of the saturated vapor pressure | 29 |
| 5.1.2 Porosity | 30 |
| 5.1.3 Light transmission evaluation | 30 |
| 5.1.3.1 Light transmission interpretations | 30 |
| 5.2 Analysis of wafer 292 | 32 |
| 5.3 Analysis of wafer 296 | 32 |
| 5.3.1 Floated membranes 296e and 296f | 33 |
| 5.3.2 Immersed membranes 296c and 296d | 34 |
| 5.4 Analysis of wafer 295 | 34 |
| 5.4.1 Membrane 295a | 35 |
| 5.4.1.1 Membrane 295a - after aluminum dissolution bath | 35 |
| 5.4.2 Membrane 295d, 295e, 295f, 295g | 36 |
| 5.4.2.1 Membrane 295g | 36 |
| 5.4.3 Membrane 295c | 36 |
| Bibliography | 44 |

List of Figures

| | | |
|------|--|----|
| 3.1 | The graph shows the pressure to diameter conversion by KELVIN equation (compare eq. (3.7)) for the parameters $T = 19^\circ\text{C}$, $\gamma_{T=19^\circ\text{C}}^{\text{hexane}} = 0,018\,605 \frac{\text{N}}{\text{m}}$ and $V_{\text{mol}, T=19^\circ\text{C}}^{\text{hexane}} = 0,130\,53 \frac{\text{L}}{\text{mol}}$ | 5 |
| 3.2 | Absorption (a) and desorption (b) isotherm of a straight cylindrical pore open on one end. The corresponding processes inside the pore are illustrated below the isotherm itself. Colors of the arrows between pore states and the respecting pressure range of the graph match. | 8 |
| 3.3 | Absorption (a) and desorption (b) isotherm of a funnelled cylindrical pore open on the large end. The corresponding processes inside the pore are illustrated below the isotherm itself. Colors of the arrows between pore states and the respecting pressure range of the graph match. | 9 |
| 3.4 | Absorption (a) and desorption (b) isotherm of a funnelled cylindrical pore open on the small end. The corresponding processes inside the pore are illustrated below the isotherm itself. Colors of the arrows between pore states and the respecting pressure range of the graph match. | 10 |
| 3.5 | Absorption (a) and desorption (b) isotherm of a straight cylindrical pore open on both ends. The corresponding processes inside the pore are illustrated below the isotherm itself. Colors of the arrows between pore states and the respecting pressure range of the graph match. | 11 |
| 3.6 | Absorption (a) and desorption (b) isotherm of a funnelled cylindrical pore open on both ends. The corresponding processes inside the pore are illustrated below the isotherm itself. Colors of the arrows between pore states and the respecting pressure range of the graph match. | 12 |
| 3.7 | Absorption and desorption isotherm loops for various kinds of cylindrical pores. For the funnelled pores it is $d > d'$ | 13 |
| 3.8 | Visual derivation of SNELL's law. | 14 |
| 3.9 | Sketch for the derivation of the FRESNEL equations. The index i stands for the incident wave, r for the reflected and t for the transmitted. The continuity of the components parallel to the $n_1 - n_2$ -interface is visualized. For the derivation please see 3.8. | 15 |
| 3.10 | balblabla | 16 |
| 3.11 | Graphical solution of the inequality eq. (3.31). While the blue shaded area also respects the inequality eq. (3.25), the orange shaded area shows the more general case $1 = n_1 < n_2, n_3$. Both cases yield a weaker transmission for the two interface transmission than for the single interface. | 17 |
| 3.12 | Using the blabla approximation for the refractive index of a nanoporous medium the transmission in its empty state is computed in section ??? | 18 |
| 4.1 | Setup for the anodizing of the membrane production. The aluminum wafer functions as anode while a platinum plate makes for the cathode. The oxalic acid is stirred during the whole process. | 20 |

| | | |
|-----|---|----|
| 4.2 | Production stages of the membrane production. It starts with a wafer of bulk aluminum (dark gray) (a) which is then anodized yielding (b), where light gray represents alumina. The latter is then dissolved producing a bulk aluminum wafer with hexagonally arranged hollows (c). By the second anodizing straight parallel pores are created (d). After dissolving the remaining aluminum (e) the barrier layer etched to open the pores (f). For the variable specifications please refer to section 4.1.1. | 21 |
| 4.3 | Setup for the aluminum dissolution step. The wafer is immersed in acid composed according to eq. (4.6) which dissolves aluminum according to section ??? | 22 |
| 4.4 | Setup for the <i>barrier layer</i> dissolution. The wafer is floated (a) or immersed (b) in phosphoric acid dissolving alumina according to section ??? . For best results a combination of floating and immersing is used (please refer to section 4.1.1.3 for clarification of <i>best</i>). | 22 |
| 4.5 | Experiment setup with bypass which allows to pump the whole system without changing the opening of the PFEIFFER microvalve. The temperatures within the reservoir and the cell are measured by the thermometers T_{res} and T_{cell} . Furthermore, P_{res} and P_{cell} are the two installed pressure gauges. The void is experimentally realized by a primary pump. | 23 |
| 4.6 | Sketch of the laser transmission setup. | 24 |
| 4.7 | Experiment setup with bypass which allows to pump the whole system without changing the opening of the PFEIFFER microvalve. The temperatures within the reservoir and the cell are measure by the thermometers T_{res} and T_{cell} . Furthermore, P_{res} and P_{cell} are the two installed pressure gauges. The void is experimentally realized by a primary pump. Furthermore, the laser transmission setup and the camera setup are outlined. Only one of the two is set in place at the same time though. | 25 |
| 5.1 | Raw volumetric isotherm data recorded with the experimental setup as explained in section 4.3 for one cycle without a membrane inside the cell and one with a membrane inside the cell. (a) shows the pressure values over time making the condensation and evaporation plateaus of absorption and desorption of hexane within the membrane's pores visible. (b) is the pressure loop which is relevant for the computation of the isotherms. Again, the before mentioned plateaus are visible as dips in the time derivative of the pressure. | 27 |
| 5.2 | (a) shows the raw data of the isotherm with membrane and interpolation of the reference isotherm without membrane. Also, the subtraction of the latter (compare integrand of eq. (5.1)) is plotted where the area to be integrated for the absorption and desorption isotherm is shaded light green. The integration according to eq. (5.3) results in the isotherm displayed in (b). | 28 |
| 5.3 | Disorder between neighboring pores during absorption (a) and desorption (b). Important is the larger degree of disorder upon the absorption process. Upon condensation pores fill immediately when the spinodal pressure $P_{\text{sp}}(d_{\min})$ is reached, where d_{\min} is the radius of the opening at the small end. The evaporation is continuous at equilibrium pressure $P_{\text{eq}}(d)$ and empties each pore simultaneously while the diameter d is large enough. | 31 |
| 5.4 | P_{rel} transmission isotherms of the membranes 292d (a), 296b (b), 295d (c), and 295f 200ALD (d). All membranes have open pores. Unlike the isotherm of membrane 292d, the transmission drops of condensation and evaporation are of the same magnitude. The magnitudes of condensation and evaporation dip are reversed in respect to membrane 292d for membrane 295f 200ALD. | 37 |
| 5.5 | MEB views of membrane 295c. The thickness of the <i>barrier layer</i> is measured directly with the ZEISS software in (a). As the membrane is not oriented exactly orthogonal to the microscope and the perspective of the layer is a bit distortet, the value can only be used as a rough approximation. (b) shows the pores on the solution side of the membrane. | 38 |

| | |
|---|----|
| 5.6 Wafer 296 processing scheme. While a signifies a recorded isotherm, the means MEB pictures have been taken. Red marks pores closed on one end, green pores open on both ends. The processed wafers are immersed in phosphoric acid for $t_{immerse}$ or floated on for t_{float} | 38 |
| 5.7 | 38 |
| 5.8 Comparison of the isotherms measured for the membranes 296a, 296e and 296f. While the pore diameters are marginally smaller for the membranes 296e and 296f than they are for 296a, the overall picture is equivalent. It makes for closed pores with the same funnelling aspect. | 39 |
| 5.9 (a) shows the isotherms of the immersion experiment conducted using wafer 296. The shift to larger pressures of the beginning of the evaporation branch and the unmoving beginning of the condensation branch are clearly visible. (b) and (c) are higher resolution plots of the relevant areas of the evaporation and respectively condensation branch of the isotherm on a pore diameter scale. For interpretations please refer to section 5.3.2. ???EXPLAIN WHY EVAP START AND COND START ARE THE SPOTS TO LOOK AT ??? | 40 |
| 5.10 Immersion of a closed pore membrane resulting in an increase of the funnelling aspect of the pores as shown in (b) due to the saturation of the acid within the pores. The visualized theory is backed by the isotherms in fig. 5.9(a) which lead to the etch rate dependency plotted in (a) on the height within a pore. For further explanations please refer to section 5.3.2. | 41 |
| 5.11 Wafer 295 processing scheme. While a signifies a recorded isotherm, the means MEB pictures have been taken. Red marks pores closed on one end, green pores open on both ends. The blue marked membranes have undergone n cycles of ALD depositing. | 41 |
| 5.12 | 42 |
| 5.13 Possible shape interpretation of the volumetric isotherms of membrane 295a for a single pore. If the interpretation were correct, an incontinuity ?? of the anodizing current could be the reason for the change in funnelling. | 42 |
| 5.14 Comparison of the isotherms of membrane 295a (closed pores) before and after a 4,5 h bath in aluminum dissolving acid (compare section 4.1.1.2). A small but homogenous shift of the isotherm to higher pressures is clearly visible. This implies that the acid does not only attack aluminum but also alumina. | 42 |
| 5.15 MEB images of membrane 295g of aluminum (a) and solution side (a). The measurements of the pore diameters were done immediately using the ZEISS software of the microscope. | 43 |

List of Tables

| | |
|--|----|
| 5.1 Diameter reduction per minute of immersion derived from the isotherms of the membranes 296a, 296c, 296d. | 34 |
|--|----|

1 Introduction

2 Introduction

2.1 Initial Goal of the Internship

Generally speaking, the goal of the internship is testing condensation and evaporation theory in confinement. The realized confinement consists of nanoporous alumina membranes absorbing and desorbing hexane while the laws to be tested are primarily the KELVIN law and the SAAM and COLE law. Furthermore, the membrane production shall be refined to the aim of creating cylindrical pores and also combining pores of different sizes to form inc bottle like confinements. The latter are to be used for studying cavitation in confinement.

2.2 Problem

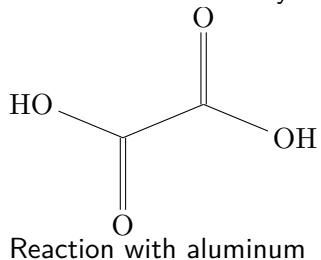
The membranes are not as good as expected in the sense, that they are not of perfect cylindrical shape and are hard to be characterized. Therefore, neither the result of the condensation and evaporation theory nor the actual shape of the pores are known. Thus, the first step must be to understand and refine the production process of the membranes. To this end, MEB views ??? are used to probe the diameter of the created pores. As the pores also show a funneling aspect and corrugations, the porosity of the membranes is also not clear. This makes the MEB view analysis less reliable to random. A way must be found to measure the porosity of the membranes and to estimate the funneling aspect

3 Theory

3.1 Chemistry

3.1.1 Oxalic Acid

Oxalic acid is a dicarboxylic acid with the formula C₂H₂O₄.



3.1.2 Phosphoric Acid

3.1.3 Aluminum Dissolution Acid

3.2 Ideal Gas Law

The ideal gas law can be written as

$$PV = nRT \quad (3.1)$$

with the pressure P , volume V , number of moles of gas n , temperature T and ideal gas constant

$$R = 8,314\,459\,8(48) \frac{\text{J}}{\text{K mol}}. \quad (3.2)$$

It is an approximation of the behaviour of gases which can be applied for sufficiently low pressures and simple atoms or molecules which do not interact strongly (for example noble gases).

3.2.1 Boyle–Mariotte Law

For a constant temperature T and constant number of moles of gas n , the ideal gas law eq. (3.1) yields the BOYLE-MARIOTTE law

$$P_1V_1 = P_2V_2. \quad (3.3)$$

It permits to measure a volume V_2 by expanding the known volume V_1 of gas and monitoring pressures P_1 and P_2 before and after the expansion.

3.3 Hexane

3.3.1 Saturated Vapor Pressure

3.3.2 Liquid Density

3.3.3 Gas Density

3.4 Laplace-Young equation

Due to the surface tension γ , the interface between two static fluids is curved. The shape of this curvature is related to the capillary pressure difference ΔP sustained across the mentioned interface by the YOUNG-LAPLACE equation

$$\begin{aligned}\Delta P &= -\gamma \cdot \nabla \hat{\mathbf{n}} \\ &= \gamma \left(\frac{1}{R_1} + \frac{1}{R_2} \right),\end{aligned}\tag{3.4}$$

with the unit vector $\hat{\mathbf{n}}$ orthogonal to the interface and the curvature radii R_1 and R_2 . The relation so implies, that the surface of a gas-liquid interface will always strive towards a homogeneous curvature to achieve an equilibrium state regarding pressure differences along the surface.

3.5 Kelvin Equation

To get to Kelvin equation from Laplace young equation one uses the equality of chemical potentials $\mu_{Liquid}(P_{liquid}) = \mu_{Gas}(P_{gas})!!!$

liquid incompressible

integration of gibss duhem realtion leads to chemical potential dependent on the density

$$dG = SdT + VdP - NdmumitT = constantV\tag{3.5}$$

$$dG = VdP - Ndmu\tag{3.6}$$

The KELVIN equation is given by

$$RT \cdot \ln \left(\frac{p_v}{p_{sv}} \right) = \gamma V_m \cdot \left(\frac{1}{r_1} + \frac{1}{r_2} \right),\tag{3.7}$$

with the gas constant R , the temperature T , p_v the vapor pressure and p_{sv} the saturated vapor pressure. Furthermore, γ is the surface tension, V_m the molar volume and r_i , $i \in \{1, 2\}$, are the radii defining the curvature of the meniscus that forms the surface of the liquid.

The conducted experiment makes use of samples with cylindrical pores. Thus, the volume's radii become

$$r_1^{\text{cyl}} = r^{\text{cyl}} < 0, \quad r_2^{\text{cyl}} \rightarrow \infty$$

for a cylindrical meniscus and

$$r_1^{\text{hsp}} = r_2^{\text{hsp}} = r^{\text{hsp}} < 0$$

for a hemispheric meniscus. Plugging these radii into equation eq. (3.7) yields the respecting KELVIN equations for a cylindrical volume

$$RT \cdot \ln \left(\frac{p_v^{\text{cyl}}}{p_{sv}} \right) = \frac{\gamma V_m}{r^{\text{cyl}}} < 0\tag{3.8}$$

$$RT \cdot \ln \left(\frac{p_v^{\text{hsp}}}{p_{sv}} \right) = 2 \cdot \frac{\gamma V_m}{r^{\text{hsp}}} < 0\tag{3.9}$$

and thus,

$$\ln\left(\frac{p_v^{\text{cyl,hsp}}}{p_v}\right) < 0 \implies p_v^{\text{cyl,hsp}} < p_v.$$

The equations eq. (3.8) and eq. (3.9) each can be solved for the radius

$$r^{\text{cyl}} = \frac{\gamma V_m}{RT} / \ln\left(\frac{p_k^{\text{cyl}}}{p_v}\right) \quad (3.10)$$

$$r^{\text{hsp}} = 2 \cdot \frac{\gamma V_m}{RT} / \ln\left(\frac{p_k^{\text{hsp}}}{p_v}\right) = 2 \cdot r^{\text{cyl}}. \quad (3.11)$$

Here, the factor of 2 between the two conversions is of much importance for the understanding of the theory of condensation and evaporation in cylindrical pores. The conversion is illustrated in fig. 3.1 for a cylindrical and a spherical meniscus (respectively the equilibrium and the spinodal mechanism). In the course of this report, the isotherms will be displayed on a

$$P_{\text{rel}} = \frac{P_v}{P_{\text{sv}}} \quad (3.12)$$

axis. Nevertheless, a lot of the analysis will be done talking pore diameters. In doubt, please refer to fig. 3.1 for a conversion.

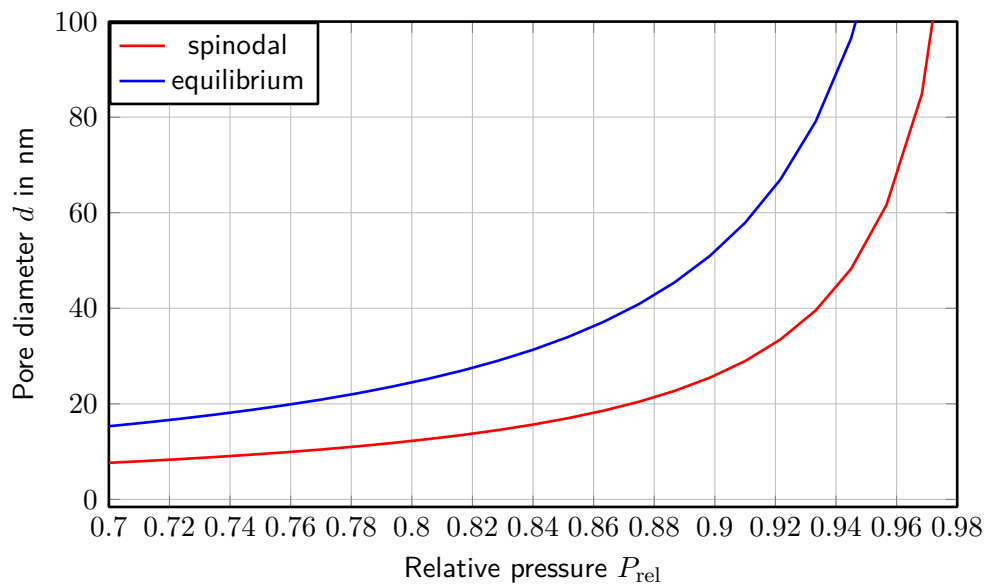


Figure 3.1 The graph shows the pressure to diameter conversion by KELVIN equation (compare eq. (3.7)) for the parameters $T = 19^\circ\text{C}$, $\gamma_{T=19^\circ\text{C}}^{\text{hexane}} = 0,018\,605 \frac{\text{N}}{\text{m}}$ and $V_{\text{mol}, T=19^\circ\text{C}}^{\text{hexane}} = 0,130\,53 \frac{\text{L}}{\text{mol}}$.

3.6 Condensation and evaporation in a cylindrical pore

To understand the condensation and evaporation of hexane in the alumina membranes, used for the conducted experiments, the processes must be understood for a single pore. The following explanation starts off with a straight cylindrical pore which is closed on one end. Then, funnelization is included in the theory. Finally, the model is applied to cylindrical pores open on both ends, straight and funnelled.

As a precondition, all pores are wetting. This means when exposed to vapor, a liquid film forms on their surface.

3.6.1 Closed pore

The term *closed pore* shall from now on be linked to a pore that is only open at one end.

3.6.1.1 Closed straight pore

The absorption isotherm of a straight cylindrical pore is illustrated in fig. 3.2 (a) with the corresponding processes inside the pore. Exposing the pore to vapor yields a wetting film on its surface (orange pressure range of the isotherm). As by LAPLACE-YOUNG eq. (3.4) different radii of menisci correspond to different pressures. Therefore, the film starts forming a spherical meniscus at the closed end of the pore (green). Upon reaching equilibrium pressure $P_{\text{eq}}(d)$ the pore fills due to the translational symmetry of the meniscus leaving only a spherical meniscus at the open end (red). The latter relaxes with increasing pressure till an even surface is left at saturated vapor pressure P_{sv} (blue).

Figure 3.2 (b) shows the corresponding desorption isotherm. When lowering the pressure from saturated vapor pressure, a spherical cap meniscus forms on the open end of the pore (orange pressure range of the isotherm). At equilibrium pressure this meniscus becomes spherical and invariant to translation inside the pore (green). Therefore, the pore empties except for a film on its surface (red). The film gets thinner with decreasing pressure and completely disappears when vacuum is reached.

3.6.1.2 Closed funneled pore - large end open

The absorption isotherm of a funnelled pore that is closed on the small end is shown in fig. 3.3 (a). Increasing the vapor pressure yields a thickening wetting film on the surface of the pore (orange pressure range of the isotherm). At the bottom of the pore a spherical cap meniscus forms that becomes a spherical meniscus at equilibrium pressure $P_{\text{eq}(r')}$ (green). At this point the pore starts to fill significantly with increasing pressure. It does not fill at one given pressure though as for the meniscus to move to larger radii, the pressure must also increase. Except for the spherical meniscus at the open end, the pore is filled at equilibrium pressure $P_{\text{eq}}(d)$. This continuous filling is implied by the red colored range of the absorption isotherm. The spherical meniscus relaxes into a spherical cap meniscus and finally transforms into an even surface at saturated vapor pressure.

The desorption isotherm is illustrated in fig. 3.3 (b). First, a spherical cap meniscus forms on the open end (orange) which transforms into a spherical meniscus upon reaching equilibrium pressure $P_{\text{eq}}(d)$ (green). At this pressure the pore begins to empty continuously till $P_{\text{eq}}(d')$ is reached (red). Only a film covering the pore's surface is left. The latter evaporates with decreasing pressure and a dry pore is left at zero pressure.

3.6.1.3 Closed funnelled pore - small end open

Figure 3.4 (a) shows the absorption isotherm of a funnelled pore that is closed at the large end. With increasing vapor pressure a film forms on the pore's surface (orange pressure range of the isotherm) and a spherical cap meniscus forms at the closed end. The latter becomes a spherical meniscus upon reaching equilibrium pressure $P_{\text{eq}}(d)$ (green). As

$$P_{\text{eq}}(d) < P_{\text{eq}}(d') \quad (3.13)$$

holds for this type of pore, the latter fills completely at this pressure. Only a spherical cap meniscus at the open end is left as the current vapor pressure, according to eq. (3.13), already exceeds the respecting equilibrium pressure. The liquids surface flattens at saturated vapor pressure.

The corresponding desorption isotherm is illustrated in fig. 3.4 (b). Decreasing the vapor pressure starting at saturated vapor pressure P_{sv} yields a spherical cap meniscus at the open end of the pore

(orange). The meniscus evolves to a spherical meniscus upon reaching equilibrium pressure $P_{\text{eq}}(d')$ (green). At this pressure, due to eq. (3.13), the pore empties completely leaving only a wetting film on its surface (red). The latter disappears in vacuum.

3.6.2 Open cylindrical pore

The term *open pore* shall from now on be linked to a pore that is open at both ends.

3.6.2.1 Open straight pore

Figure 3.5 (a) shows the desorption isotherm of an open pore of straight cylindrical shape and the corresponding processes inside the pore. As a wetting pore of diameter d is regarded, a film of liquid appears on the inside of the pore at low pressures already (orange pressure range of the isotherm). The latter forms a cylindrical meniscus. Upon increasing the pressure, the film thickens in correspondence to the green pressure range of the isotherm. Reaching the spinodal pressure $P_{\text{sp}}(d)$, the films collapse yielding a filled pore with menisci at either open end (red). The menisci are spherical cap menisci as

$$P_{\text{eq}}(d) < P_{\text{sp}}(d) < P_{\text{sv}} \quad (3.14)$$

holds for this type of pore, where $P_{\text{eq}}(d)$ is the equilibrium pressure and P_{sv} the saturated vapor pressure. The menisci relax upon further increasing the pressure and finally transform into even surfaces at saturated vapor pressure (blue).

The desorption isotherm of a straight cylindrical pore is illustrated in fig. 3.5 (b). Again, the corresponding processes inside the pore are illustrated below. At first, spherical cap menisci form on either end of the filled pore (orange). Upon reaching equilibrium pressure $P_{\text{eq}}(d)$ these menisci are spherical (green) and invariant regarding translation along the pore axes. Moreover, the vapor is not saturated yet, so the pore empties leaving only a film of liquid on the inside of the pore (red). The film gets thinner with decreasing pressure and disappears at saturated vapor pressure (blue).

As condensation and evaporation for a perfect cylindrical pore occur on two different values of vapor pressure, the spinodal pressure P_{sp} and the equilibrium pressure P_{eq} , the process yields a hysteresis. A complete isothermal loop of condensation and evaporation is shown in fig. 3.7.

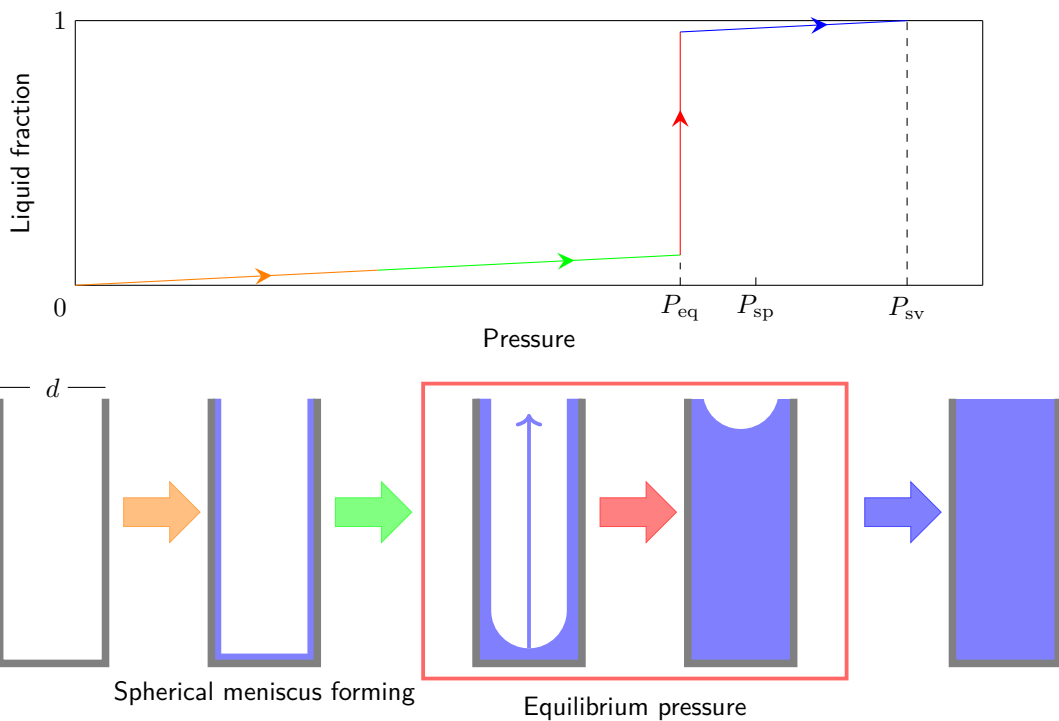
3.6.2.2 Open funnelled pore

Here, a funnelled cylindrical pore that is open at both ends is regarded. A precondition shall be that the funnelization is small in respect to the pore's diameter, in explanation

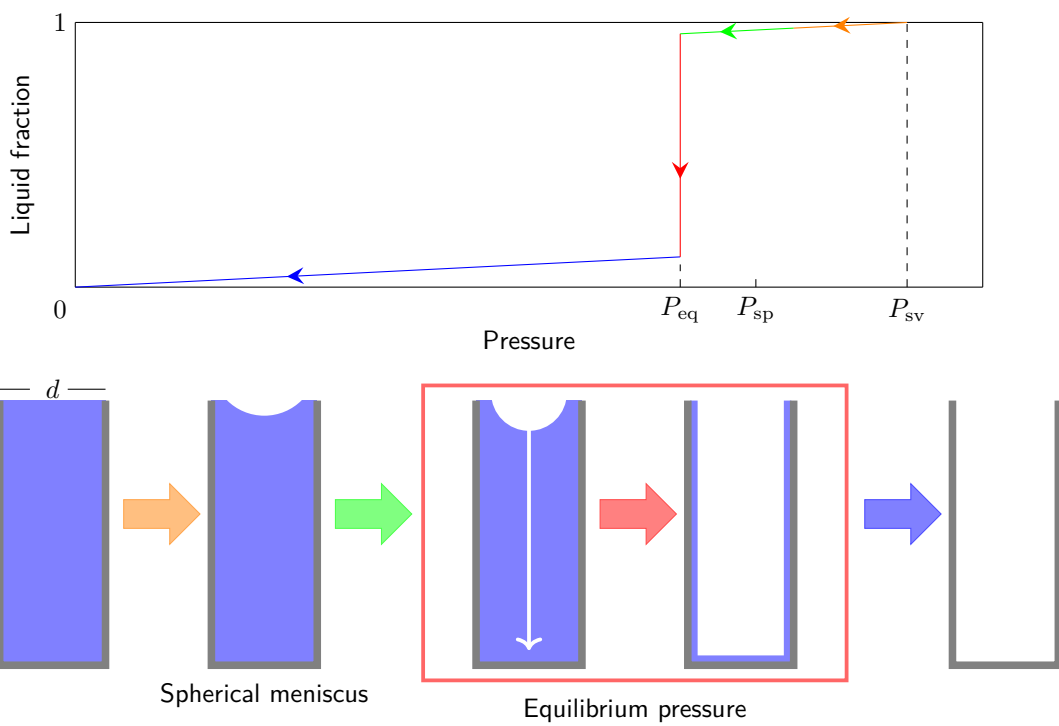
$$P_{\text{sp}}(d') \geq P_{\text{eq}}(d). \quad (3.15)$$

The absorption isotherm is illustrated in fig. 3.6 (a). Exposed to vapor, the surface of the pore wets leaving a thickening film (orange and green pressure range of the isotherm). At spinodal pressure $P_{\text{sp}}(d')$, the films collapse on the small end of the pore yielding a closed pore. The liquid bridge forms spherical menisci on both sides and in reference to eq. (3.15), the pore fills completely leaving only a spherical cap meniscus at each end. These relax when further increasing the vapor pressure and disappear at saturated vapor pressure P_{sv} .

Figure 3.6 (b) shows the desorption isotherm of the regarded pore. Spherical cap menisci form at both ends when reducing the vapor pressure from saturated vapor pressure (orange pressure range of the isotherm). Upon reaching equilibrium pressure $P_{\text{eq}}(d)$, the meniscus on the large end transforms into a spherical meniscus (green). Then, the pore starts to continuously empty from the large end with decreasing pressure. At $P_{\text{eq}}(d')$, only a wetting film is left on the surface of the pore (red). This film disappears at zero pressure (blue).

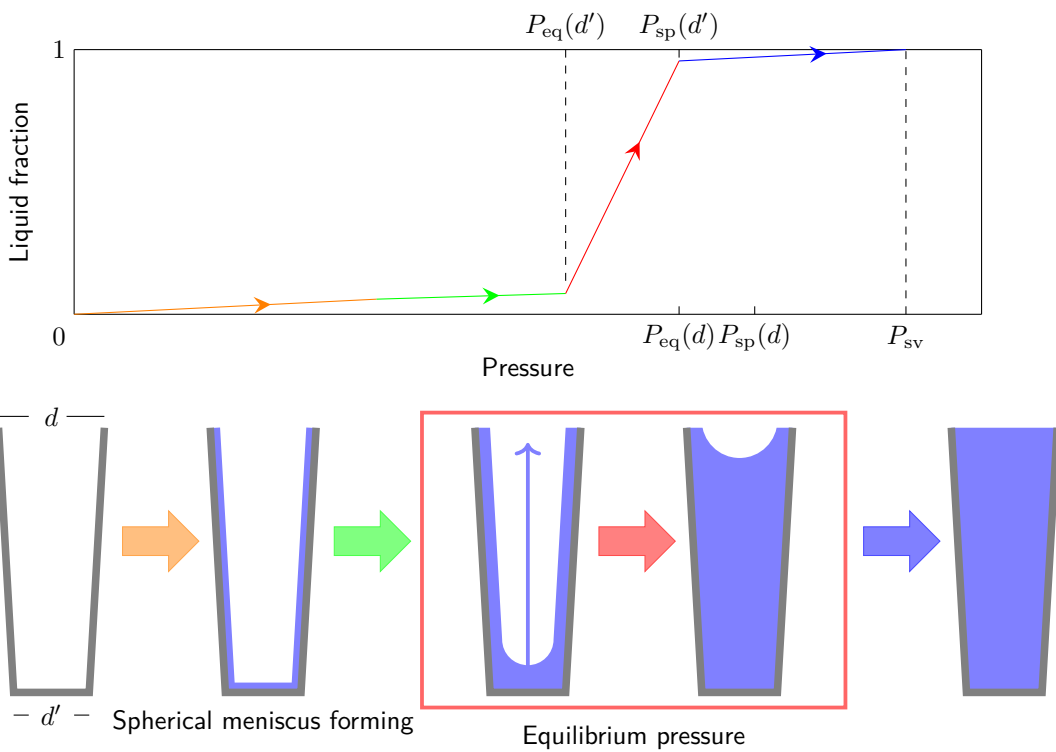


(a) Absorption isotherm. Significant is the absorption at equilibrium pressure.

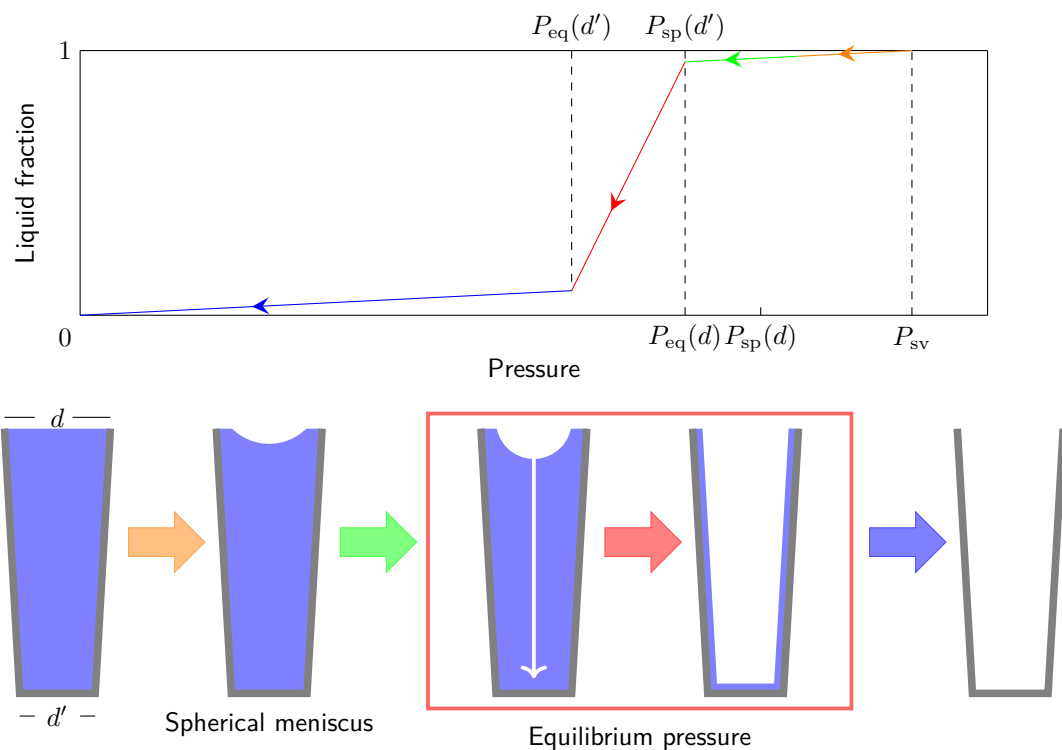


(b) Desorption isotherm. Significant is the desorption at equilibrium pressure.

Figure 3.2 Absorption (a) and desorption (b) isotherm of a straight cylindrical pore open on one end. The corresponding processes inside the pore are illustrated below the isotherm itself. Colors of the arrows between pore states and the respecting pressure range of the graph match.

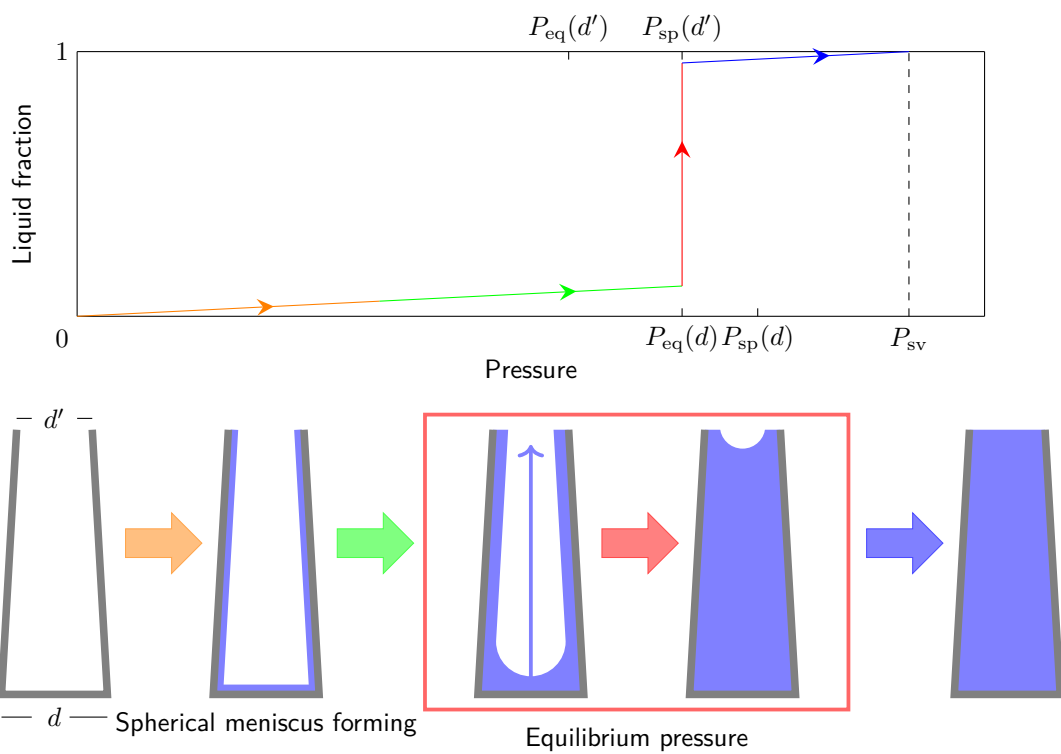


(a) Absorption isotherm. Significant is the absorption at equilibrium pressure.

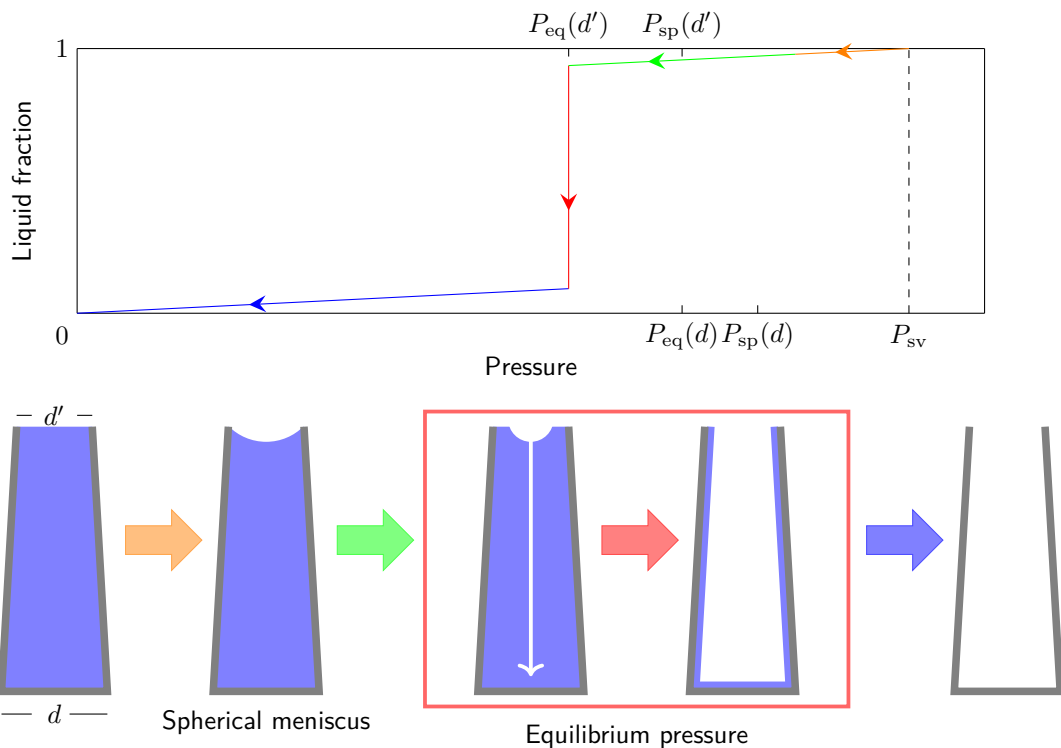


(b) Desorption isotherm. Significant is the desorption at equilibrium pressure.

Figure 3.3 Absorption (a) and desorption (b) isotherm of a funnelled cylindrical pore open on the large end. The corresponding processes inside the pore are illustrated below the isotherm itself. Colors of the arrows between pore states and the respecting pressure range of the graph match.

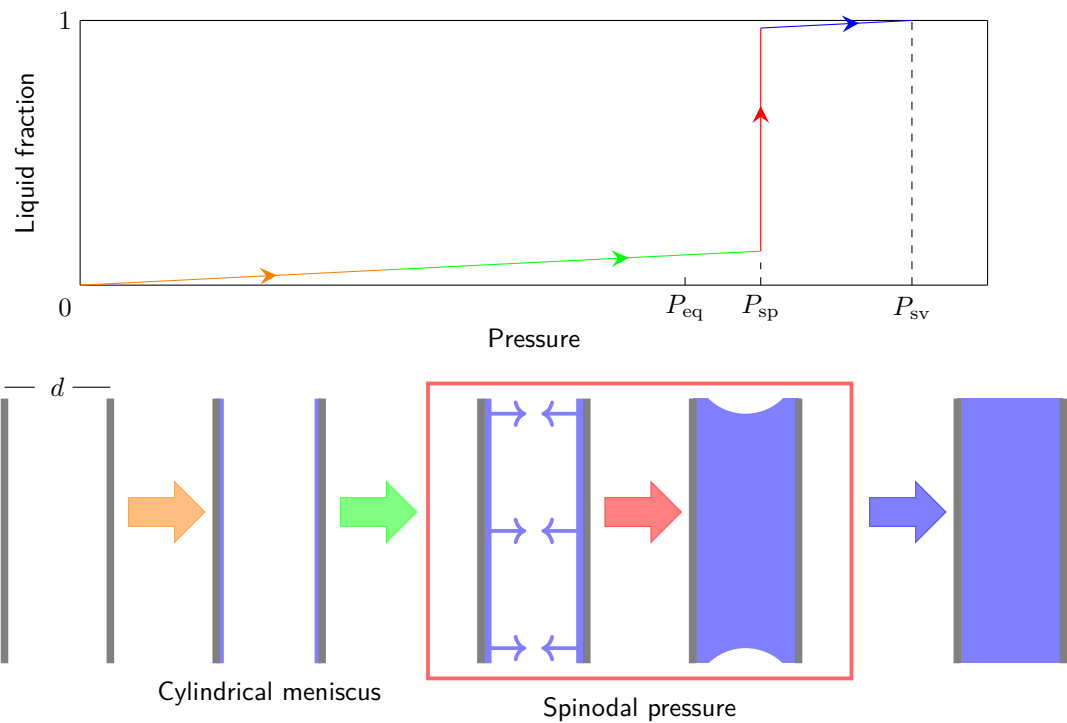


(a) Absorption isotherm. Significant is the absorption at equilibrium pressure $P_{eq}(d)$.

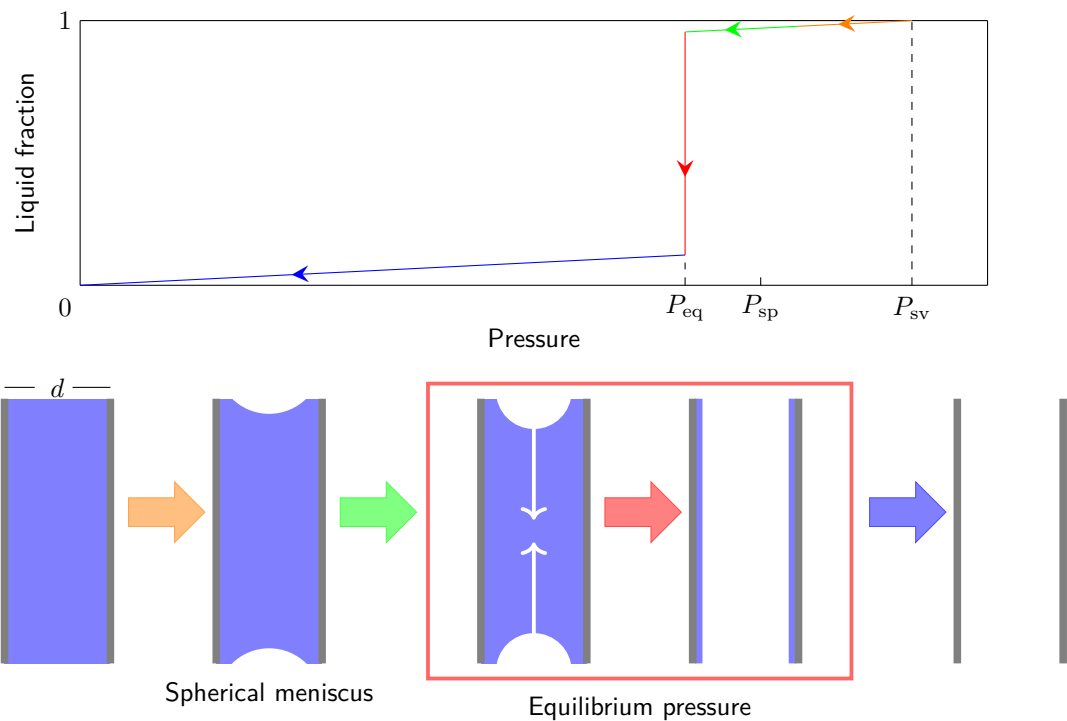


(b) Desorption isotherm. Significant is the desorption at equilibrium pressure $P_{eq}(d')$.

Figure 3.4 Absorption (a) and desorption (b) isotherm of a funnelled cylindrical pore open on the small end. The corresponding processes inside the pore are illustrated below the isotherm itself. Colors of the arrows between pore states and the respecting pressure range of the graph match.

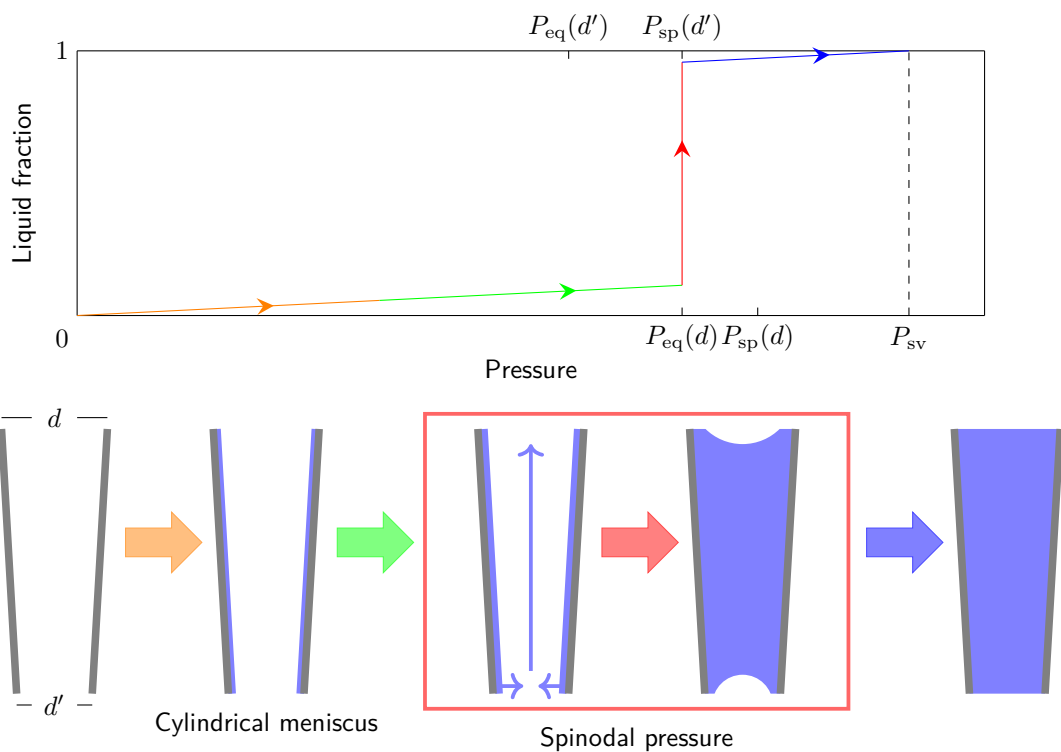


(a) Absorption isotherm. Significant is the absorption at spinodal pressure.

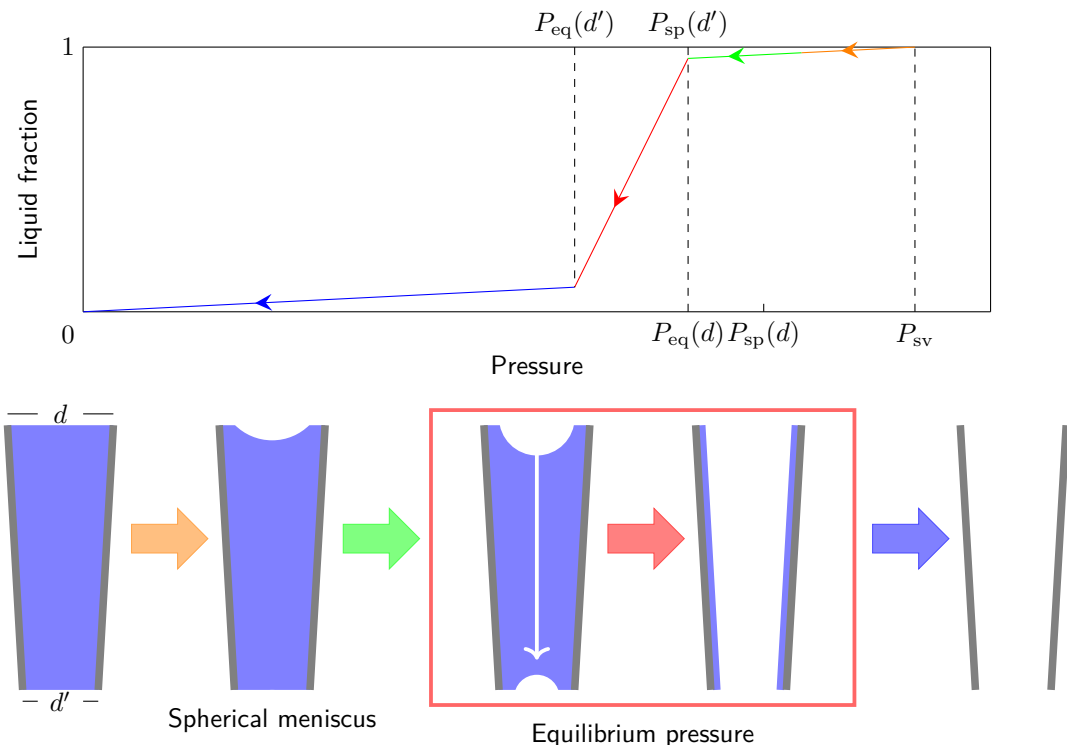


(b) Desorption isotherm. Significant is the desorption at equilibrium pressure.

Figure 3.5 Absorption (a) and desorption (b) isotherm of a straight cylindrical pore open on both ends. The corresponding processes inside the pore are illustrated below the isotherm itself. Colors of the arrows between pore states and the respecting pressure range of the graph match.

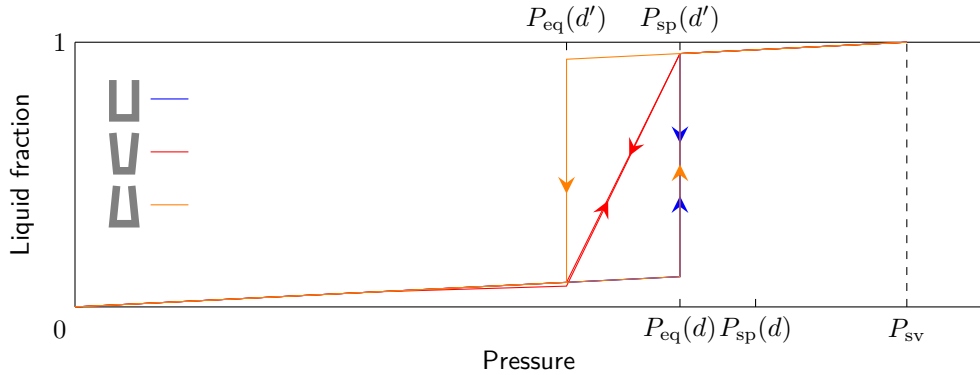


(a) Absorption isotherm. Significant is the absorption at spinodal pressure $P_{\text{sp}}(d') \geq P_{\text{eq}}(d)$.

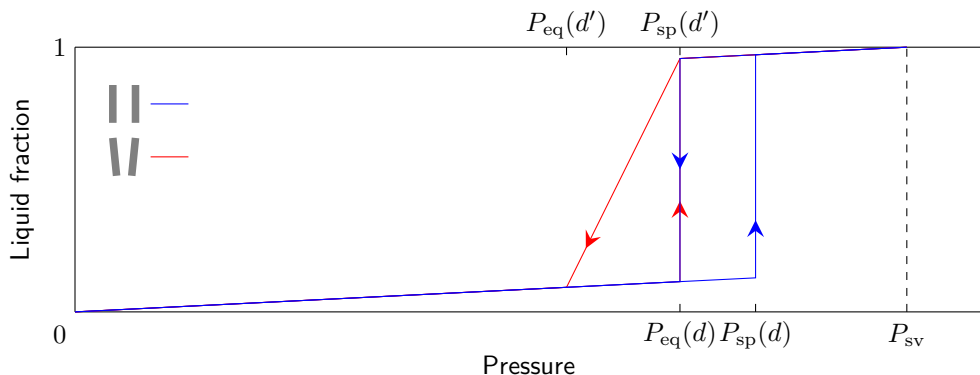


(b) Desorption isotherm. Significant is the continuous desorption at the equilibrium pressures $P_{\text{sp}}(d)$ to $P_{\text{sp}}(d')$.

Figure 3.6 Absorption (a) and desorption (b) isotherm of a funnelled cylindrical pore open on both ends. The corresponding processes inside the pore are illustrated below the isotherm itself. Colors of the arrows between pore states and the respecting pressure range of the graph match.



(a) Cylindrical pore open on one end.



(b) Cylindrical pore open on both ends.

Figure 3.7 Absorption and desorption isotherm loops for various kinds of cylindrical pores. For the funnelled pores it is $d > d'$.

3.6.3 Isotherm comparison

From the previous sections a resume as to which kind of pore yields which kind of absorption and desorption isotherm loop can be concluded. The loops for closed pores are shown in fig. 3.7 (a), those for closed pores in (b). Closed pores do not necessarily result in a hysteresis, open pores do so.

3.7 Snell's Law

The law of refraction by SNELL describes relation between the angles of incidence and refraction of an electromagnetic wave that passes from a medium with refractive index n_1 to a medium with the index n_2 . It is derived from FERMAT's principle, which implies that an electromagnetic wave traveling from point A to point B always takes the fastest path possible. Using the dependency of the speed of light on the index of refraction of a medium

$$v_i = \frac{c}{n_i}, \quad (3.16)$$

according to figure fig. 3.8, the wave takes the time

$$t = \frac{\sqrt{x^2 + a^2}}{v_1} + \frac{\sqrt{(l-x)^2 + b^2}}{v_2} \quad (3.17)$$

to travel from A to C . To find the shortest possible time depending on the parameter x , equation eq. (3.17) is derived and equated to zero yielding the SNELL's law

$$n_1 \sin(\alpha) = n_2 \sin(\beta). \quad (3.18)$$

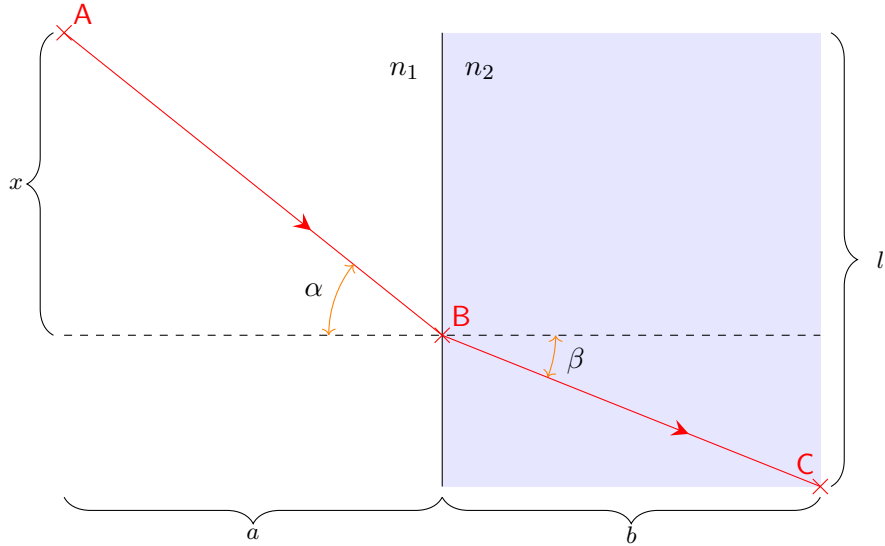


Figure 3.8 Visual derivation of SNELL's law.

3.8 Fresnel Equations

The FRESNEL equations describe the transmission and reflection coefficients of an electromagnetic wave passing from a medium with a refractive index n_1 to a medium with refractive index n_2 . They are derived from the MAXWELL equations and the SNELL's law as follows. An electromagnetic wave hitting an interface as described above is partially reflected and partially transmitted. The law of reflection yields the reflection angle

$$\theta_r = \theta_i, \quad (3.19)$$

where θ_i is the incident angle (compare figure fig. 3.9). Moreover, the transmitted part behaves according to SNELL's law resulting in the angle θ_t (section section 3.7). In the following, only o-polarized waves shall be regarded. The MAXWELL equations yield the electromagnetic boundary conditions

$$\begin{aligned} E_i \cos \theta_i + E_r \cos \theta_i &= E_t \cos \theta_t \\ H_i - H_r &= H_t. \end{aligned} \quad (3.20)$$

In words, the components of the magnetic field H_{\parallel} and the electric field E_{\parallel} are continuous. Using

$$\begin{aligned} H &= \sqrt{\frac{\epsilon}{\mu}} E \\ n &= c \sqrt{\epsilon \mu} \end{aligned} \quad (3.21)$$

to solve the equations eq. (3.20) yields the FRESNEL equations

$$\begin{aligned} r_p &= \frac{E_r^p}{E_i^p} = \frac{\frac{n_1}{\mu_1} \cos \theta_t - \frac{n_2}{\mu_2} \cos \theta_i}{\frac{n_1}{\mu_1} \cos \theta_t + \frac{n_2}{\mu_2} \cos \theta_i} \\ t_p &= \frac{E_t^p}{E_i^p} = \frac{2 \frac{n_1}{\mu_1} \cos \theta_t}{\frac{n_1}{\mu_1} \cos \theta_t + \frac{n_2}{\mu_2} \cos \theta_i}. \end{aligned} \quad (3.22)$$

Assuming non magnetic materials, in explanation

$$\mu_1 = \mu_2 \mu_0, \quad (3.23)$$

and using SNELL's law to simplify, eq. (3.22) becomes

$$\begin{aligned} r_p &= \frac{n_1 \cos \theta_t - n_2 \cos \theta_t}{n_1 \cos \theta_t + n_2 \cos \theta_t} \\ t_p &= \frac{2n_1 \cos \theta_i}{n_1 \cos \theta_t + n_2 \cos \theta_t}. \end{aligned} \quad (3.24)$$

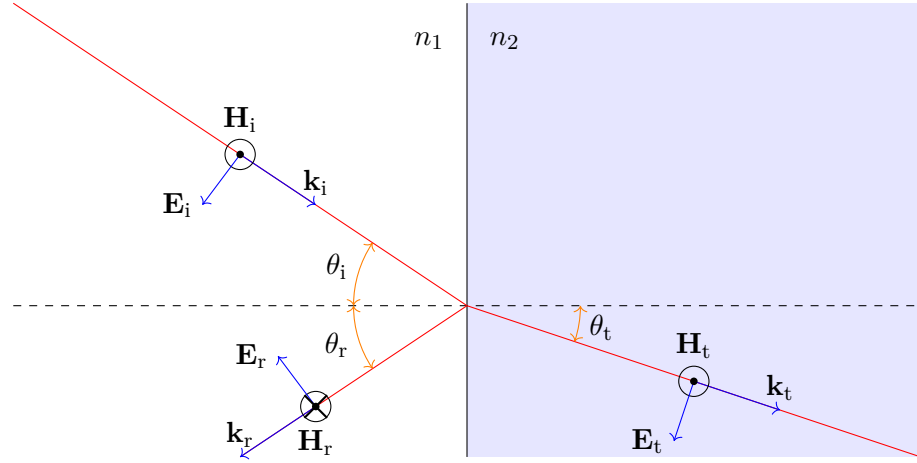


Figure 3.9 Sketch for the derivation of the FRESNEL equations. The index i stands for the incident wave, r for the reflected and t for the transmitted. The continuity of the components parallel to the n_1 - n_2 -interface is visualized. For the derivation please see 3.8.

3.8.1 Two Interface Transmission

In this section, the transmission of an electromagnetic wave through two media of increasing refractive indices

$$1 = n_1 < n_2 < n_3 \quad (3.25)$$

shall be compared to that a single interface transmission with

$$1 = n_1 < n_3. \quad (3.26)$$

Figure fig. 3.10 shows the two situations and defines the respective angles. To simplify the situation further

$$\alpha = 0 \quad (3.27)$$

shall be assumed as the incident angle. Hereby, the FRESNEL transmission coefficient eq. (3.24) becomes

$$t_p = \frac{2n_1}{n_1 + n_2} \quad (3.28)$$

as by SNELL's law eq. (3.27) makes for

$$\alpha = \beta = \gamma = \delta = 0. \quad (3.29)$$

Because more diffracting matter is added to the system, the two interface transmission is expected to yield a lower transmission than the single interface transmission, even though refractive index contrasts

$$\Delta n = n_i - n_j, \quad \{i, j\} \in \{1, 2, 3\}, \quad (3.30)$$

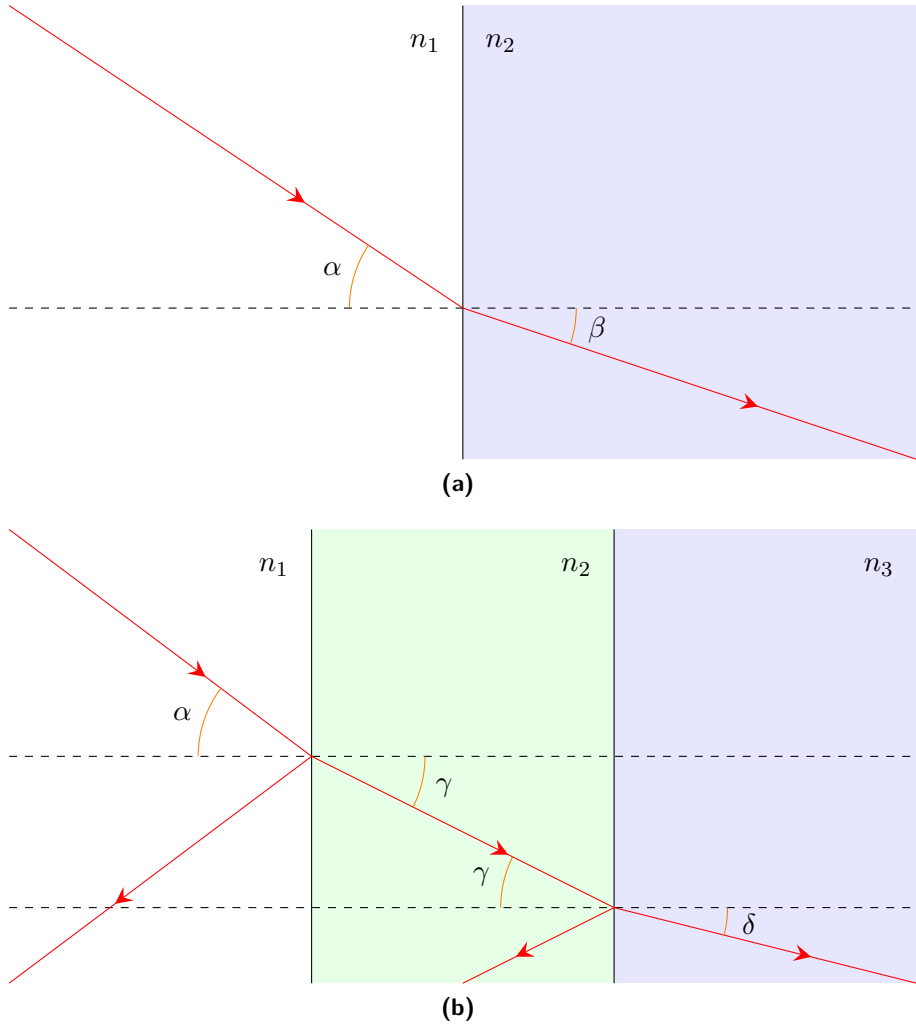


Figure 3.10 balblabla

are smaller. Therefore, the inequality

$$\begin{aligned} t_p^{13} &> t_p^{123} = t_p^{12} \cdot t_p^{23} \\ \frac{2n_1}{n_1 + n_3} &> \frac{2n_1}{n_1 + n_2} \cdot \frac{n_2}{n_2 + n_3} \end{aligned} \quad (3.31)$$

is regarded. With figure fig. 3.11 eq. (3.31) is solved graphically. The yielded result is that the transmission of the two interface transmission is indeed weaker than for the single interface assuming the inequality eq. (3.25).

3.9 Blablabla Näherung

The refractive index of a porous medium with structures in the range of the wavelength of the transmitting light can be approximated by the blablabla???. Using the porosity $0 < \phi < 1$ as a parameter it is assumed that the effective refractive index behaves like

$$n_{\text{eff}} = n_1 (1 - \phi) + n_2 \phi \quad (3.32)$$

where $n_{1,2}$ are the indices of the two components the medium is composed off (for nanoporous alumina membranes in empty state the components are alumina and vacuum for example).

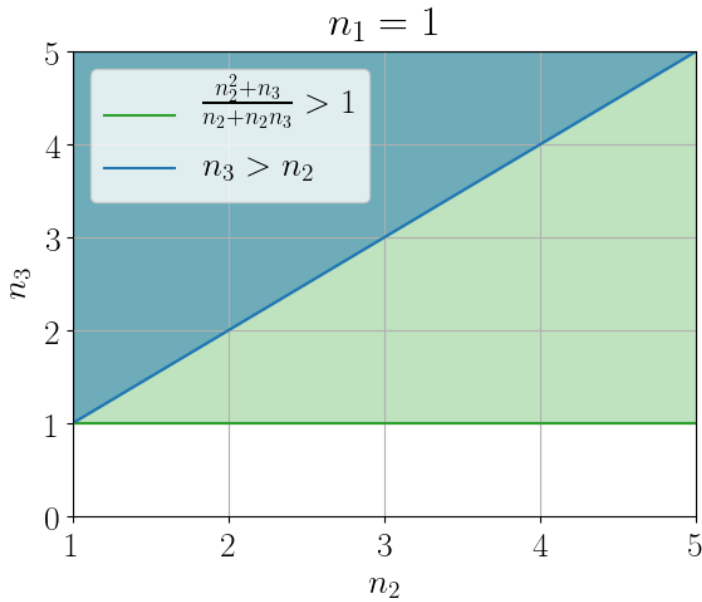


Figure 3.11 Graphical solution of the inequality eq. (3.31). While the blue shaded area also respects the inequality eq. (3.25), the orange shaded area shows the more general case $1 = n_1 < n_2, n_3$. Both cases yield a weaker transmission for the two interface transmission than for the single interface.

3.9.1 Transmission of Nanoporous Membranes in Empty and Filled State

Here, nanoporous media made of an arbitrary material with the sole condition that $n_{\text{mat}} > 1$ shall be regarded in empty and filled state. The wetting liquid's refractive index be $n_{\text{liq}} > 1$. The approximation eq. (3.32) yields the inequality

$$n_{\text{eff}}^{\text{empty}} = n_1 \cdot (1 - \phi) + n_{\text{vac}} \cdot \phi < n_1 (1 - \phi) + n_{\text{liq}} \phi = n_{\text{eff}}^{\text{filled}}, \quad (3.33)$$

where

$$1 = n_{\text{vac}} < n_{\text{liq}} \quad (3.34)$$

with the refractive index of vacuum n_{vac} . Referring to eq. (3.24) yields the transmission coefficients

$$T_{\text{empty}} = \left(\frac{2n_{\text{vac}}}{n_{\text{vac}} + n_{\text{eff}}^{\text{empty}}} \right)^2 \stackrel{\text{eq. (3.33)}}{>} \left(\frac{2n_{\text{vac}}}{n_{\text{vac}} + n_{\text{eff}}^{\text{filled}}} \right)^2 = T_{\text{filled}} \quad (3.35)$$

when assuming an incident angle $\theta_i = 0$ once again.

3.9.1.1 Transmission of Empty AAM Membrane

To give an example, the transmission coefficient of an empty nanoporous alumina membrane as used in the conducted experiments is computed in the following. The alumina membranes parameters are

$$\phi = 25 \% \quad (3.36)$$

$$n_{\text{Al}_2\text{O}_3} = 1,7682 \quad (3.37)$$

which make for a transmission coefficient of

$$T_{\text{Al}_2\text{O}_3}^{\text{empty}} = 0,9024. \quad (3.38)$$

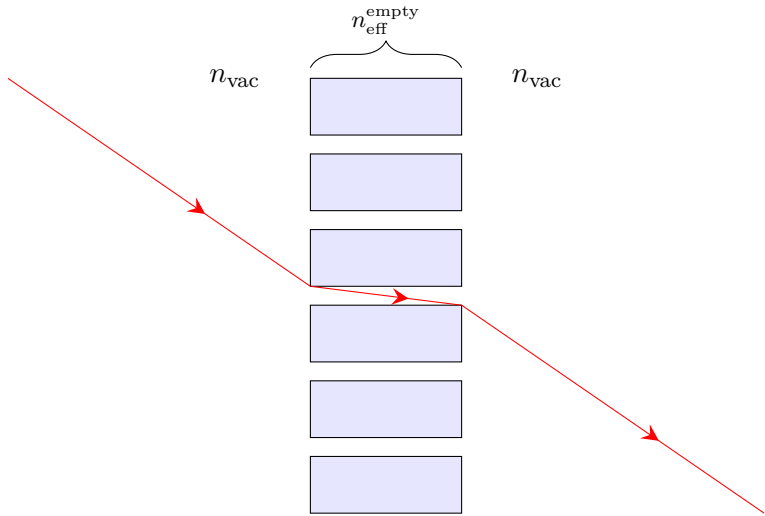


Figure 3.12 Using the blabla approximation for the refractive index of a nanoporous medium the transmission in its empty state is computed in section ???.

3.10 Rayleigh Scattering

3.11 Index Matching

4 Experimental

4.1 Alumina Membranes

4.1.1 Membrane Production

The alumina membrane production process starts with a circular wafer of amorphous aluminum of 99,999 % purity. With an initial thickness of $h_{\text{Al}} = 1 \text{ mm}$ and diameter of $d_{\text{wafer}} = 5 \text{ cm}$, one wafer is cut into twelve square membranes of side length $l_{\text{membrane}} = 1 \text{ cm}$.

First, the aluminum is anodized to create parallel pores that are arranged in a hexagonal order (compare section section 4.1.1.1). For the conducted experiment, pore lengths $l_{\text{pore}} = 30 \mu\text{m}$ and $60 \mu\text{m}$ are used. After the anodizing, the remaining aluminum of the wafer is dissolved by immersion in as specified in eq. (4.6) in section 4.1.1.2). Last, the so called *barrier layer* closing the pores on the bottom end is etched using oxalic acid (section section 4.1.1.3).

4.1.1.1 Anodizing

Figure 4.1 shows a sketch of the anodizing setup. The bulk aluminum wafer (compare fig. 4.2(a)), which functions as the anode, is glued to a copper plate using none conductive silver paste. Only one circular surface is exposed to the acid. The cathode is given by a platinum plate that is placed at a horizontal distance of 3 cm from the anode. The whole setup is immersed in oxalic acid that is stirred at all times. The anodizing of the wafers is conducted at a constant voltage $U_{\text{anodizing}}$. To produce parallel pores, the anodizing is carried out in two stages. Both use the same setup with the same parameters.

The pore diameter d_{pore} and the inter pore distance $d_{\text{interpore}}$ depends on the anodizing conditions, in explanation the voltage $U_{\text{anodizing}}$, the oxalic acid's molar concentration $n_{\text{C}_2\text{H}_2\text{O}_4}$ and the acid temperature $T_{\text{C}_2\text{H}_2\text{O}_4}$. Feasible are diameters of 10 nm to 100 nm. To produce wafers with the pore specifications

$$\begin{aligned} d_{\text{pore}} &= 40 \text{ nm}, \\ d_{\text{interpore}} &= 100 \text{ nm}, \end{aligned} \tag{4.1}$$

the parameters

$$\begin{aligned} U_{\text{anodizing}}^{40 \text{ nm}} &= 40 \text{ V}, \\ n_{\text{C}_2\text{H}_2\text{O}_4} &= 0,5 \frac{\text{mol}}{\text{l}}, \\ T_{\text{C}_2\text{H}_2\text{O}_4} &= 15^\circ\text{C} \end{aligned} \tag{4.2}$$

are used for the two anodizings. This makes for a growth rate of alumina of

$$r_{\text{Al}_2\text{O}_3} \approx 8 \frac{\mu\text{m}}{\text{s}}. \tag{4.3}$$

The first anodizing treats the raw bulk aluminum wafer. By the oxalic acid $\text{C}_2\text{H}_2\text{O}_4$, pathways are etched into the aluminum which follow no pattern at first. Only some of them continue to grow

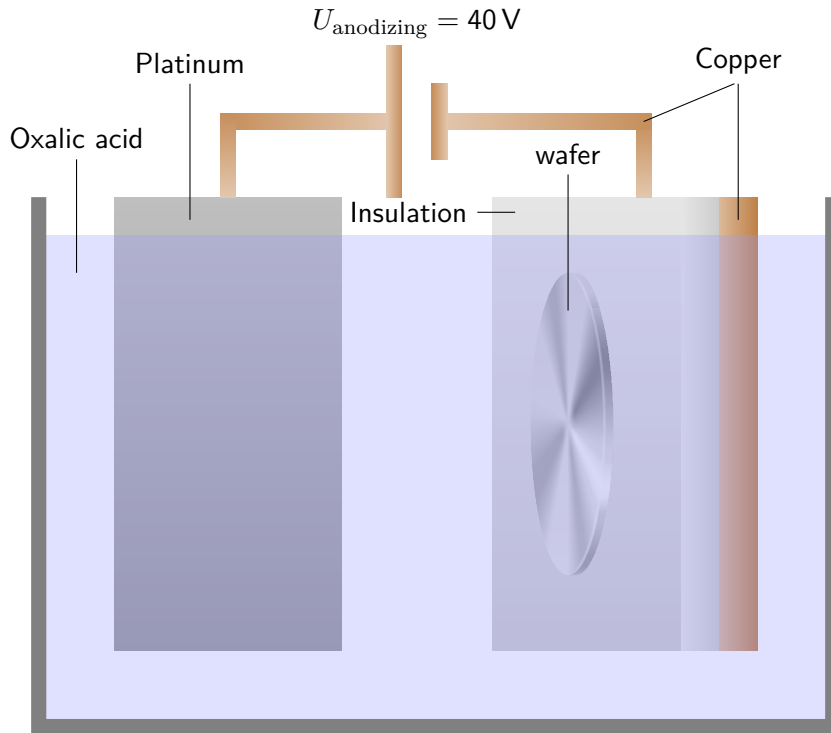


Figure 4.1 Setup for the anodizing of the membrane production. The aluminum wafer functions as anode while a platinum plate makes for the cathode. The oxalic acid is stirred during the whole process.

forming real pores, though. With the ongoing anodizing pores start to combine to form larger pores and finally areas of hexagonally arrange pores are created throughout the wafer. The longer the anodizing process is carried out, the larger these ordered areas become. Figure fig. 4.2(b) shows the cross-section of a wafer observable at this point. Because the process transforms aluminum to alumina (compare section ???) at a given penetration speed, the so called *barrier layer* of alumina separates the pores from the bulk aluminum.

Before the second anodizing, the wafer is immersed in a mixture of chromic and phosphoric acid with the concentrations

$$\begin{aligned} n_{\text{H}_3\text{PO}_4} &= 0,4 \frac{\text{mol}}{\text{l}} \\ n_{\text{C}_2\text{O}_3} &= 0,2 \frac{\text{mol}}{\text{l}} \end{aligned} \quad (4.4)$$

at a temperature of

$$T_{\text{C}_2\text{O}_3}^{\text{H}_3\text{PO}_4} = 0,2 \frac{\text{mol}}{\text{l}} \quad (4.5)$$

Hereby the created alumina is dissolved. This yields a slightly thinner wafer of bulk aluminum, where the thickness d'_{Al} depends on the time of the first anodizing. The relevant difference to the initial wafer are the areas of hexagonally arranged hollows (compare figure fig. 4.2(c)).

Due to this new surface structure, the second anodizing yields a wafer with a top layer of alumina penetrated by parallel, hexagonally arranged pores. Again, the *barrier layer* of alumina separates the pores from the bulk aluminum as illustrated in figure fig. 4.2(d). Increasing the time of the second anodizing increases the length of the pores l_{pore} and hereby the thickness of the final wafer. As the second anodizing is carried out under the same conditions as the first, the pore size d_{pore} is the same in both production steps.

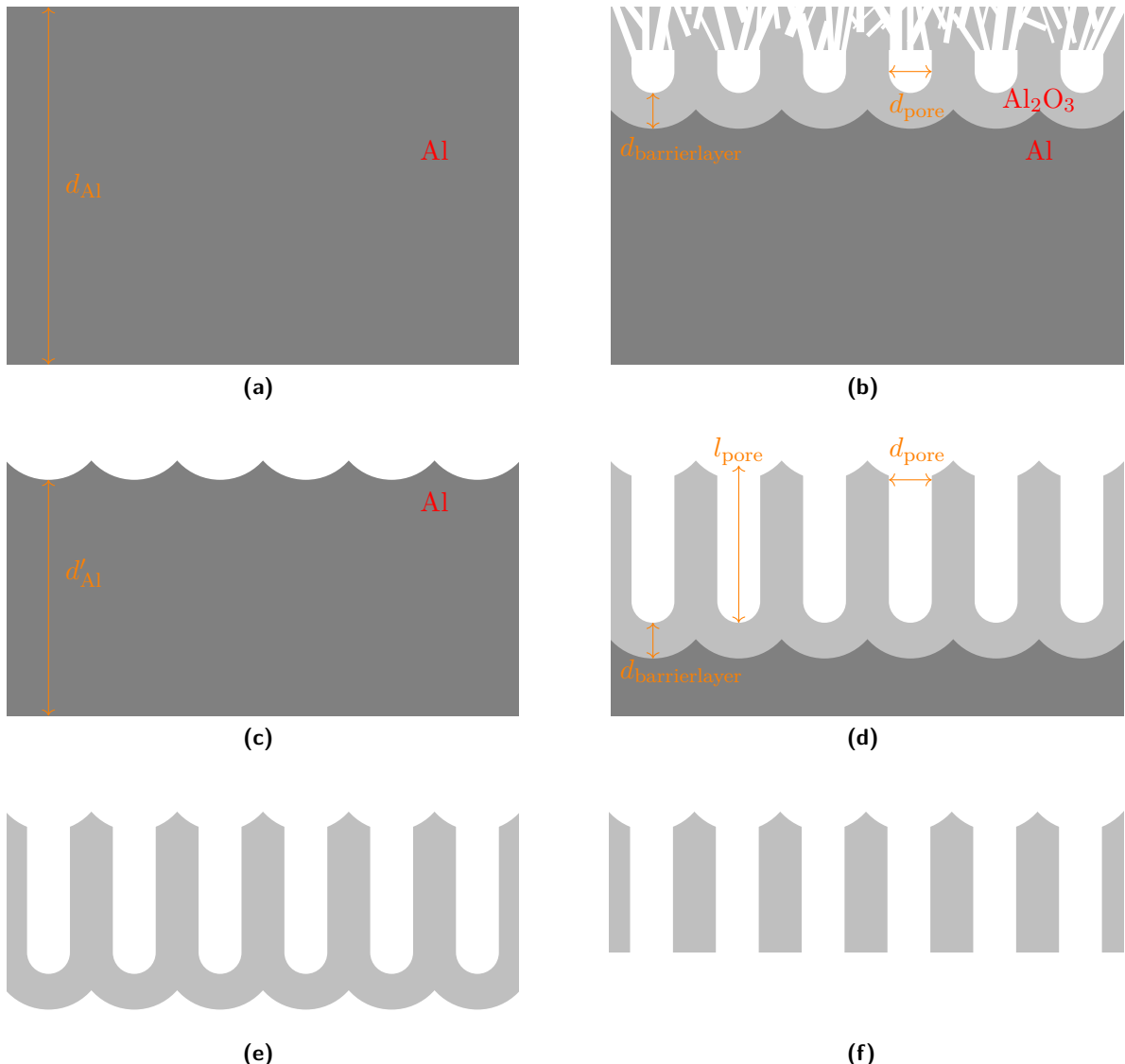
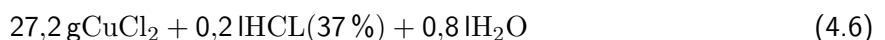


Figure 4.2 Production stages of the membrane production. It starts with a wafer of bulk aluminum (dark gray) (a) which is then anodized yielding (b), where light gray represents alumina. The latter is then dissolved producing a bulk aluminum wafer with hexagonally arranged hollows (c). By the second anodizing straight parallel pores are created (d). After dissolving the remaining aluminum (e) the barrier layer etched to open the pores (f). For the variable specifications please refer to section 4.1.1.

4.1.1.2 Aluminum Dissolution

To dissolve the remaining aluminum on the bottom side of the wafer, it is immersed in an acid composed of



at a temperature of

$$T = 0^\circ\text{C} \quad (4.7)$$

as shown in figure fig. 4.3. The latter transforms the aluminum to copper in a very exothermic reaction (compare section ???). A lot of turbulences are created and thus this step limits either the thickness or the size of the wafers because it can easily break.

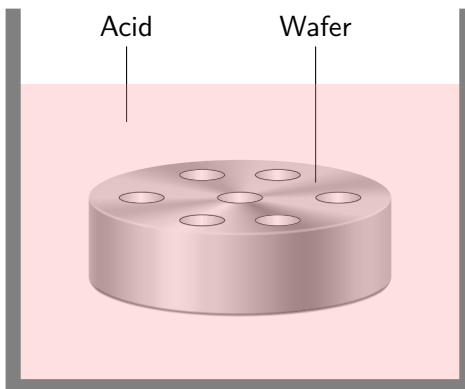


Figure 4.3 Setup for the aluminum dissolution step. The wafer is immersed in acid composed according to eq. (4.6) which dissolves aluminum according to section ???.

4.1.1.3 Barrier Layer Dissolution

The *barrier layer* dissolution is one step of the membrane production chain that is taken a closer look at in this report. The procedure is done using phosphoric acid of the concentration

$$n_{\text{H}_3\text{O}_4\text{P}} = 0,2 \frac{\text{mol}}{\text{l}}. \quad (4.8)$$

To dissolve the *barrier layer* and hereby open the pores, the wafers are floated on phosphoric acid as shown in figure fig. 4.4(a). Moreover, some membranes are immersed (compare fig. 4.4(b)) in the run of the experiments with the same aim of dissolving the *barrier layer*. If not explicitly mentioned though, the dissolution process has been conducted by floating for the respective membrane.

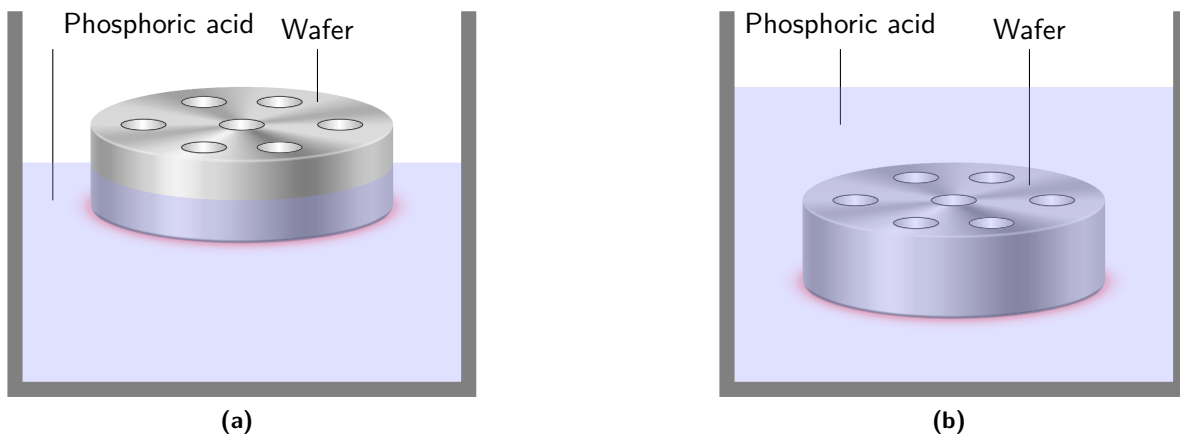


Figure 4.4 Setup for the *barrier layer* dissolution. The wafer is floated (a) or immersed (b) in phosphoric acid dissolving alumina according to section ????. For best results a combination of floating and immersing is used (please refer to section 4.1.1.3 for clarification of *best*).

4.1.2 Membrane Specifications

For the experiments, square alumina membranes of DRAW A NICE IMAGE OF A MEMBRANE AND A PORE HERE???

4.2 Experimental setup

The experimental setup consists of two independent parts. To record isotherms, the core of the experiment is the volumetric measurement conducted in the setup explained in section 4.2.1. In addition to that, there are a light transmission setup and a camera setup that can be set up one at a time. Both setups are used to monitor what happens during the absorption and desorption isotherms using optics. While the camera setup provides for a visual interpretation of the occurrences, the data acquired by the light transmission measurement is used to measure the heterogeneities of the processes and put it in context with the volumetric isotherms.

4.2.1 Volumetric setup

The initial volumetric setup is sketched in fig. 4.5. A thermostatted bath by LAUDA functions as a reservoir of bulk hexane and is connected to the rest of the experiment via a valve. Behind the valve lies a cross leading to a pressure gauge P_{res} , via another valve to a primary pump (void), and via a PFEIFFER microvalve to the cell containing the sample membrane. This branch is also connected to a pressure gauge P_{cell} . The microvalve is the key part of the experiment as it allows for the extremely low flow rates that are necessary for the conducted experiment (section 4.3). Furthermore, the temperature of the cell and that of the thermostatted bath are monitored by the thermometers T_{cell} and T_{res} .

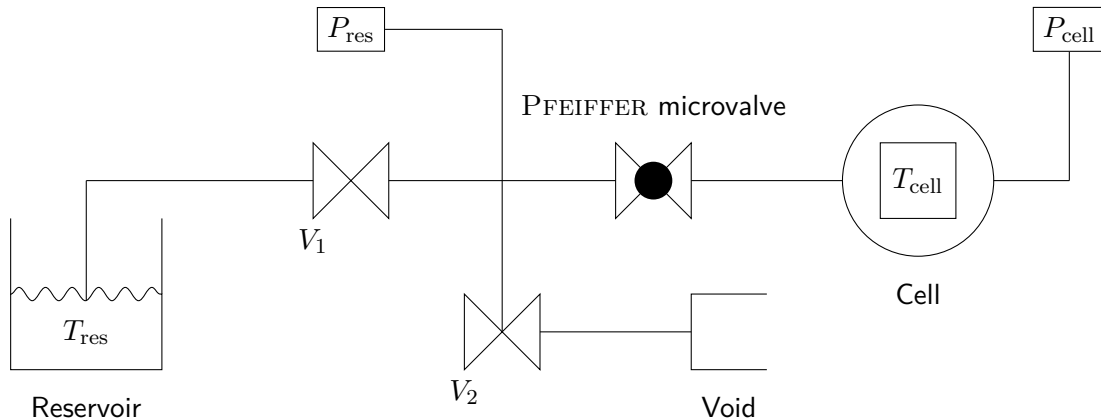


Figure 4.5 Experiment setup with bypass which allows to pump the whole system without changing the opening of the PFEIFFER microvalve. The temperatures within the reservoir and the cell are measured by the thermometers T_{res} and T_{cell} . Furthermore, P_{res} and P_{cell} are the two installed pressure gauges. The void is experimentally realized by a primary pump.

The whole experiment setup is placed in a climatized room set to

$$T_{\text{room}} = 23^\circ\text{C}. \quad (4.9)$$

The coldest point of the experiment must be the cell containing the sample membrane as to be sure no hexane condenses anywhere else in the setup. Therefore, the temperature of the cell is regulated to

$$T_{\text{cell}} = 19^\circ\text{C} \quad (4.10)$$

as explained in section 4.2.1.1 while the reservoir of bulk hexane is set to a temperature of

$$T_{\text{res}} = 21^\circ\text{C} \quad (4.11)$$

using the LAUDA.

4.2.1.1 Cell temperature regulation

The cell itself is made of a copper ring which is sealed on both sides using sapphire windows. Making use of indium O-rings, the windows are pressed onto the the copper ring by two aluminum rings. This circular cell is designed so it can be mounted to a second copper construction which is connected to a PELTIER heat pump and a heater. Moreover, two thermometers installed - one for the temperature regulation feedback loop and one for the output value. While the power of the PELTIER is fixed, the heater's power output is controlled by the feedback loop. From the microvalve to the pressure gauge P_{cell} , the setup is packed in styrofoam for thermal insulation from the room temperature and also to minimize the gradient inside this part of the setup. At first, the regulation has been run via a regular computer. As this led to breakdowns of the regulation for short periods of time multiple times per hour, the regulation was then externalized to an RASPBERRY PI. It regulates the temperature to $T_{\text{cell}} = 19,000(5) \text{ }^{\circ}\text{C}$.

4.2.1.2 Pressure gauges

Because of its high resolution, at first, a KELLER S21 ??? pressure gauge was used for P_{cell} . As its construction contains a porous O'ring that could be identified as the source of degassing inside the system, the gauge has been swapped for a WIKA ??? which exposes only metallic parts to the system. P_{res} uses the same model of pressure gauge.

4.2.2 Laser transmission setup

The laser transmission setup is sketched out in fig. 4.6. In the path of the initial laser beam, a collimator and a diaphragm are placed before the cell. After being RAYLEIGH scattered by the membrane (please refer to section 5.1.3 for explanations), the beam then passes another diaphragm and a collecting lense before hitting the photodiode.

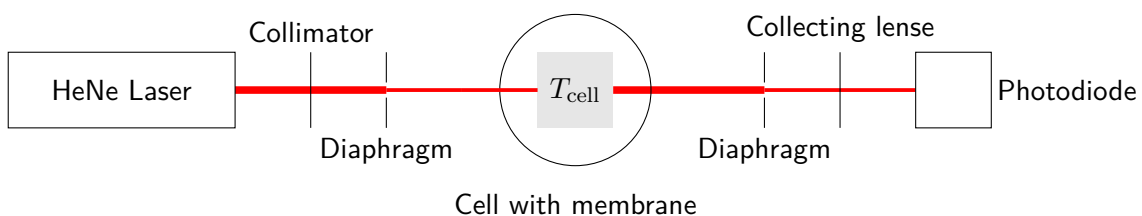


Figure 4.6 Sketch of the laser transmission setup.

4.2.3 Camera setup

To record images of the membranes during the absorption and desorption isotherms, a camera is installed and focused on the alumina membrane. A ???MODEL??? is used without any further optical instruments.

4.3 Experimental procedure

To start an experiment (here also referred to as an isotherm) the valve U_1 is closed while U_2 and the PFEIFFER microvalve U_{PV} are fully opened. This allows the primary pump, which experimentally realizes the void, to pump the system. As the condensation of hexane inside the sample starts at a pressure of about 150 mbar, it is not import to reach low pressures in this step. On the other hand

the pumping is used to clean the system of air which unavoidably enters the system when places the membrane inside the cell (or removing it from of the cell).

After pumping the system, U_2 is closed and the condensation process initialized by setting U_{PV} to a sufficiently low opening voltage and opening U_1 . Sufficiently low opening voltage shall imply that the condensation plateau of the condensation inside the membrane's pores is distinguishable on the recorded P over t isotherm. The employed flow rate's magnitude is $10^{-5} \frac{\text{mbar l}}{\text{s}}$.

To also record the bulk condensation plateau, which defines the saturated vapor pressure P_{sv} in the evaluation process, the setup is left condensing inside the cell for five hours after the pressure inside the cell reaches $P_{cell} = 150 \text{ mbar}$. This way a small amount of bulk liquid is condensed inside the cell. At the end of the process, all the valves are closed.

The evaporation process is then initialized by opening the valve U_2 . Meanwhile, the PFEIFFER microvalve is set to a sufficiently low opening voltage U_{PV} to permit the primary pump to pump the system. Again, sufficiently low implies that the evaporation plateau of the liquid evaporating from the membrane's pores is visible on the recorded P over t isotherm. The system is left in this state till the pressure inside the cell P_{cell} reached a given setpoint at which the microvalve is fully opened to pump the system and prepare for another isotherm.

4.3.1 Bypass

As the flow rate of hexane in the system only depends on the opening of the PFEIFFER microvalve and the pressures P_{res} and P_{cell} , this opening should always be the same to be able to compare multiple isotherms. Due to the uncertainty of the microvalve showing some hysteresis upon opening and closing, a bypass is added to the setup. As shown in fig. 4.7, the new setup allows to pump the part of the system containing the cell without changing the opening of the PFEIFFER microvalve now. This way there is no need to ever change the before mentioned opening and one potential error source is removed from the system.

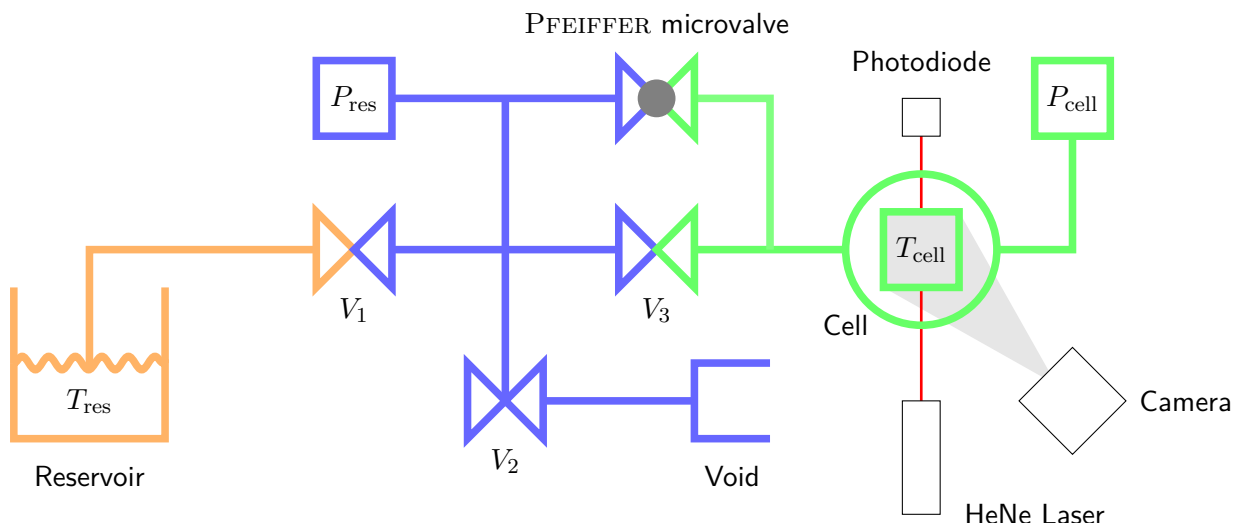


Figure 4.7 Experiment setup with bypass which allows to pump the whole system without changing the opening of the PFEIFFER microvalve. The temperatures within the reservoir and the cell are measure by the thermometers T_{res} and T_{cell} . Furthermore, P_{res} and P_{cell} are the two installed pressure gauges. The void is experimentally realized by a primary pump. Furthermore, the laser transmission setup and the camera setup are outlined. Only one of the two is set in place at the same time though.

The green volume of the system, which is the one of interest for the isotherm computation, is calibrated using the method explained in section section 3.2.1. Its volume is

$$V_{cell} = 8,27 \text{ cm.} \quad (4.12)$$

4.3.1.1 Changing the membrane

To change the sample, the copper cell must be opened and therefore detached from the rest of the system. After placing the membrane to be measured inside the cell, the latter is then reconnected to the system. As a result, the inside of the cell is at atmospheric pressure. Before the bypass was installed, to pump the cell, the PFEIFFER microvalve had to be opened. Using the small opening also used for the isotherms would have made for an unbearably long pumping process. For an approximation please refer to fig. 5.1(a) in section 5.1 where hexane is pumped from the system. As the evaluation of the volumetric measurements depends strongly on the opening of the PFEIFFER microvalve which is not guaranteed to reopen without a hysteresis even if the same voltage as before is applied, the bypass has been installed to create a way to pump the system without touching the PFEIFFER's opening. From this point on, the contamination of the cell with degassing grease and the VCR connectors, that do leak to a certain degree are the most prominent hazards of the membrane changing process.

5 Analysis

5.1 Computing the isotherms

To compute the isotherms from the recorded data the experiment needs to be conducted not only with a membrane inside of the cell, but also with an empty cell. From here on, the following indices shall be used:

- 1 → no membrane
- 2 → membrane.

Furthermore, the variables P_i , \dot{P}_i , V_i , T_i , n_i and \dot{n}_i , $i \in \{1, 2\}$, refer to the values measured inside of the cell, in explanation the red marked part of the system in fig. 4.7. The raw isotherms of the two experiments are shown in fig. 5.1. The plateaus of the yellow curve with membrane inside the cell of the plot versus time correspond to the dips of the time derivative of the pressure of the versus pressure plot. This can be explained by the hexane condensing inside the membrane's pores at a given pressure due to which the continuing matter flow into the cell does not yield an increase of pressure.

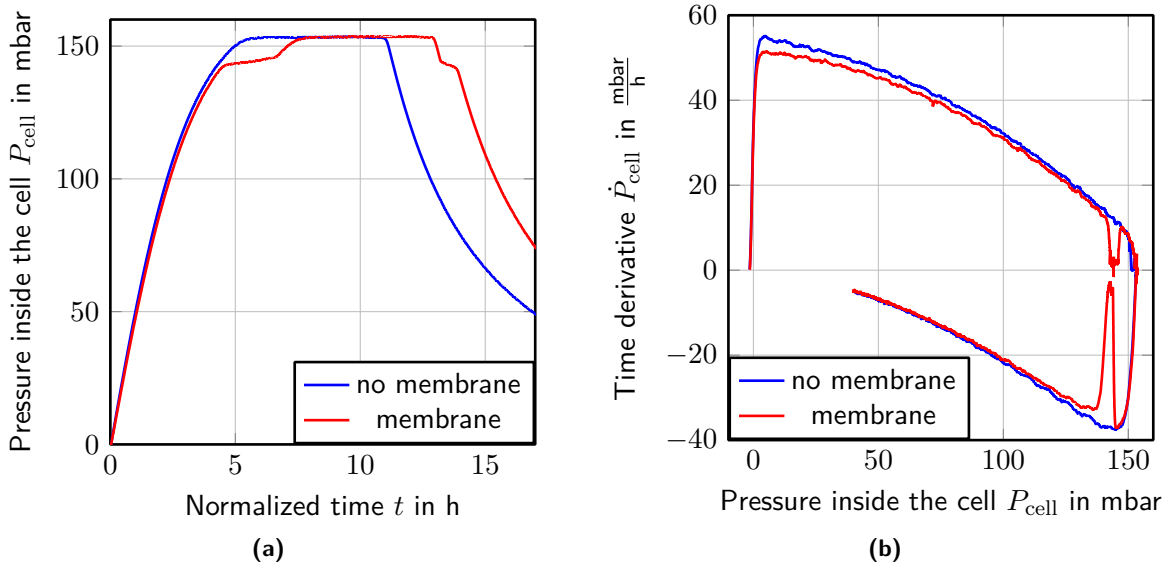


Figure 5.1 Raw volumetric isotherm data recorded with the experimental setup as explained in section 4.3 for one cycle without a membrane inside the cell and one with a membrane inside the cell. (a) shows the pressure values over time making the condensation and evaporation plateaus of absorption and desorption of hexane within the membrane's pores visible. (b) is the pressure loop which is relevant for the computation of the isotherms. Again, the before mentioned plateaus are visible as dips in the time derivative of the pressure.

Regarding the system with an empty cell, it is clear that the ideal gas law can be used to compute the flow rate of hexane (compare section 3.2). By solving for the amount of matter

$$n_1 = \frac{P_1 V_1}{R T_1},$$

taking into account that the temperature of the cell is regulated at T_1 and the volume V_1 is constant, the flow of matter becomes

$$\dot{n}_1 = \frac{V_1}{RT_1} \cdot \dot{P}_1.$$

Furthermore, the flow of matter for the system with a membrane inside the cell can be interpreted as the sum of the flow into the membrane \dot{n}_2^{mem} and the flow into the system volume excluding the membrane \dot{n}_2^{cell} . This can be rewritten yielding

$$\dot{n}_2^{\text{mem}} = \dot{n}_2 - \dot{n}_2^{\text{cell}},$$

where \dot{n}_2^{cell} obeys ideal gas law. Using the fact that the flow through the PFEIFFER valve only depends on the pressure difference $\Delta P_i = P_i^{\text{tank}} - P_i^{\text{cell}}$, assuming that $P_1^{\text{tank}} = P_2^{\text{tank}}$ leads to

$$\begin{aligned} \dot{n}_2^{\text{mem}}(P_2) &= \dot{n}_1(P_2) - \dot{n}_2^{\text{cell}}(P_2) \\ &= \frac{V_1}{RT_1} \cdot \dot{P}_1(P_2) - \frac{V_2}{RT_2} \cdot \dot{P}_2(P_2) \end{aligned} \quad (5.1)$$

Figure 5.2(a) shows the computation steps visually using the respective plots versus time.

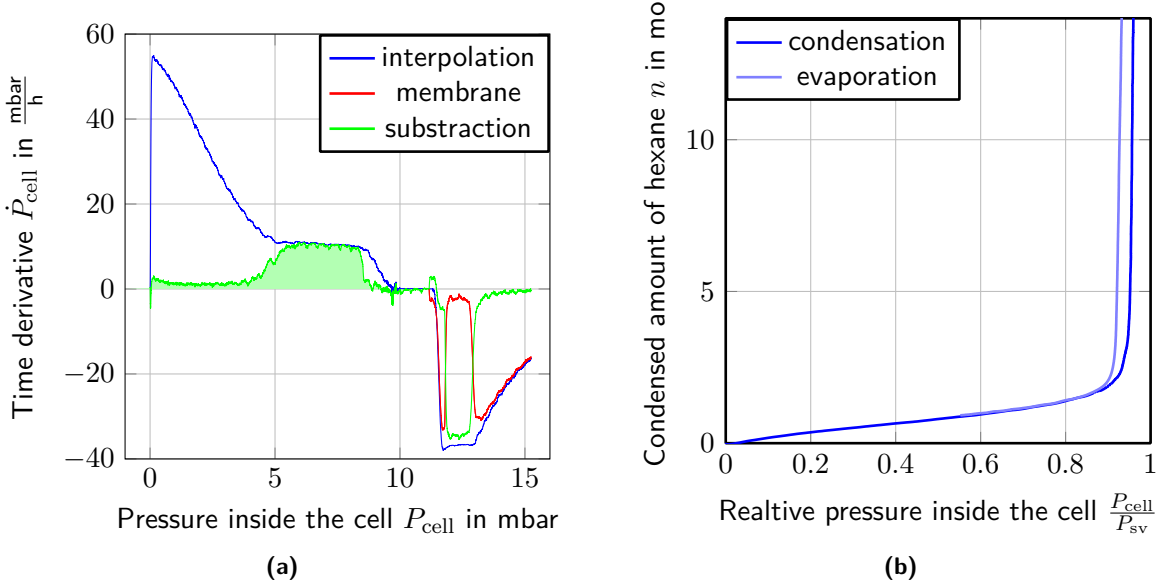


Figure 5.2 (a) shows the raw data of the isotherm with membrane and interpolation of the reference isotherm without membrane. Also, the subtraction of the latter (compare integrand of eq. (5.1)) is plotted where the area to be integrated for the absorption and desorption isotherm is shaded light green. The integration according to eq. (5.3) results in the isotherm displayed in (b).

As the temperature of the system is regulated ($T = T_1 = T_2 = \text{const.}$) and because $V = V_1 \approx V_2$ since $V_{\text{mem}} \ll V_1$, equation eq. (5.1) yields

$$n_2^{\text{membrane}} = \frac{V}{RT} \int_0^{t_2} (\dot{P}_1(t'_1) - \dot{P}_2(t'_2)) dt'_2. \quad (5.2)$$

Important at this point is the dependency of $\dot{P}_1(t_1)$ on t_1 while the integration is over t_2 .

As the experimental setup yields discrete values at given time intervals Δt , the data evaluation makes use of a sum rather than an integration.

$$n = \frac{V}{RT} \sum (\dot{P}_1(P_1 = P_2) - \dot{P}_2(P_2)) \cdot \Delta t \quad (5.3)$$

yields the molar amount of hexane condensed inside the membrane. Figure fig. 5.2(b) shows the result of the integration eq. (5.3) for membrane 296d. It is an absorption and desorption isotherm for

hexane inside the porous alumina membrane. The bulk condensation and evaporation is not visible, as it is also recorded with the reference isotherm without membrane inside the cell.

What stings the eye is that the sharp rise of the condensation branch does not start at the liquid fraction $LF = 0$. The same goes for the evaporation branch. It only drops to a liquid fraction value $LF > 0$ and then decreases superimposed with the condensation branch. While it would be reasonable to renormalize the graph so only the mentioned sharp rise and drop are relevant for the isotherm as this part is where the pores fill or empty at spinodal or equilibrium pressure (section 3.6), it is not done here. The reason for this is that the initial rise of the isotherms is assumed to be due to the build up of a film on the membranes surfaces. This is part of the theory of condensation and evaporation in confinement even though the film is ignored in the basic KELVIN equation (section 3.5). ???MAKE A COMPUTATION AS TO HOW MANY MOLES OF LIQUID ARE EXPECTED FOR THE FILMS ON ONE SINGLE MEMBRANE???

Moreover, the plots

$$i \text{ over } j, \quad i \in \{n, LF, FF\}, \quad j \in \{P_{\text{cell}}, P_{\text{rel}}, D_{\text{kelvin}}\} \quad (5.4)$$

are of interest, where

$$P_{\text{rel}} = \frac{P_{\text{cell}}}{P_{\text{sv}}^{\text{exp}}}, \quad (5.5)$$

with the saturated vapor pressure P_{sv} .

$$LF = \frac{n}{n_{\text{max}}} \quad (5.6)$$

is the liquid fraction of hexane condensed inside the pores of the membrane using the total maximum amount of condensed hexane n_{max} and last,

$$FF = \frac{V_{\text{hex}}^{\text{cond}}}{V_{\text{mem}}} \quad (5.7)$$

with the volume of condensed hexane $V_{\text{hex}}^{\text{cond}}$ and the membrane's volume V_{mem} , is the filled fraction of the membrane. Its maximum corresponds to the porosity of the membrane. For the computation please refer to section 5.1.2.

For the computation of the introduced physical sizes, the saturated vapor pressure P_{sv} must be determined.

5.1.1 Determination of the saturated vapor pressure

As the bulk condensation plateau shows a slight drift (compare figure fig. 5.1), using the maximum measured pressure P_{cell} does not yield the saturated vapor pressure P_{sv} but a higher value. In addition, depending on the contamination of the system by air or degassing grease, the measured value for P_{sv} shifts due to the partial pressures. To probe the reproducibility of an isotherm loop including the grade of contamination, the node[anchor=south]maximum measured pressure for different membranes is compared. As the system is opened to replace the membrane in between the isotherms, each cycle is independent. For the change of membrane process please read section 4.3.1.1. The result of the experiment is that $P_{\text{sv}}^{\text{exp}}$ fluctuates by

$$\delta P_{\text{sv}}^{\text{exp}} = \pm 0,5 \text{ mbar}. \quad (5.8)$$

As the relevant plateau of condensation and evaporation inside the pores of the membrane occur at about

$$P_{\text{plateaus}} = 140 \text{ mbar}, \quad (5.9)$$

$\delta P_{\text{sv}}^{\text{exp}}$ translates to an error of about

$$\delta P_{\text{rel}} \leq \pm 0,005. \quad (5.10)$$

5.1.2 Porosity

Equation eq. (5.3) gives the molar amount of hexane n_{hex} condensed inside the membrane's pores. Furthermore, for the given pressures 0 mbar to 160 mbar hexane in its liquid form can be regarded as incompressible and therefore the hexane's volume be computed via

$$V_{\text{hex}} = n_{\text{hex}} \cdot V_{\text{mol,hex}}.$$

. The thickness l_{pore} of the membrane is easily determinable via MEB views since its magnitude is micrometers. Finally, the area A_{mem} of the measured samples is derived from a photo taken using binoculars.

Using these information the porosity ϕ of a given membrane is given by

$$\phi = 1 - \frac{V_{\text{hex}}}{V_{\text{mem}}}, \quad (5.11)$$

with the membrane's volume

$$V_{\text{mem}} = A_{\text{mem}} \cdot l_{\text{pore}}.$$

5.1.3 Light transmission evaluation

As mentioned in section 4.2, the light transmission setup is independent from the volumetric measurements and also the evaluations do not depend on each other. The light transmission is rather a tool to check on the theory of evaporation and condensation within the membrane using a different approach.

To compute the transmission coefficient of a membrane, it is measured in dry state using the same transmission setup as during the volumetric experiment yielding $T_{\text{mem}}^{\text{dry}}$. Then, the first measured intensity value I_0 of a given isotherm is assigned to the dry coefficient as at this point no hexane is condensed inside of the membranes pores yet. From there on, each intensity measurement is translated to a transmission coefficient according to

$$T(t) = T_{\text{mem}}^{\text{dry}} \cdot \frac{I_0}{I(t)}. \quad (5.12)$$

The aquired physical size can be interpreted as explained in the following section 5.1.3.1.

As a forword shall be mentioned that the observed transmission drops' magnitude cannot be explained by simple media transmissions as explained in section 3.8.1. Even counting multiple transitions for a diagonal transmission of a membrane, the regular transmission is not a sufficient explanation as the filled state of a membrane should by that theory be less transmitting than the empty state whereas the opposite is observed. To explain the phenomena, RAYLEIGH scattering and index matching, which are explained in section 3.10 and section 3.11 respectively, must be taken into account.

5.1.3.1 Light transmission interpretations

Firstly, a completely filled membrane should always yield a higher transmission coefficient T than in its dry state according to the theory of index matching explained in section 3.11. This fact serves as a tool to optically detect membranes that do not fill completely due to constrictions.

Furthermore, due to the disorder created by pore filling and emptying, the transmission drops during the processes. Phenomena occurring on the volumetric measurements can therefore be interpreted corresponding to the measured transmission coefficient.

Last, an often observed phenomenon is that the transmission drops to lower values for the condensation than for evaporation of a given isotherm. Figure 5.4 shows an isotherm of membrane 292d

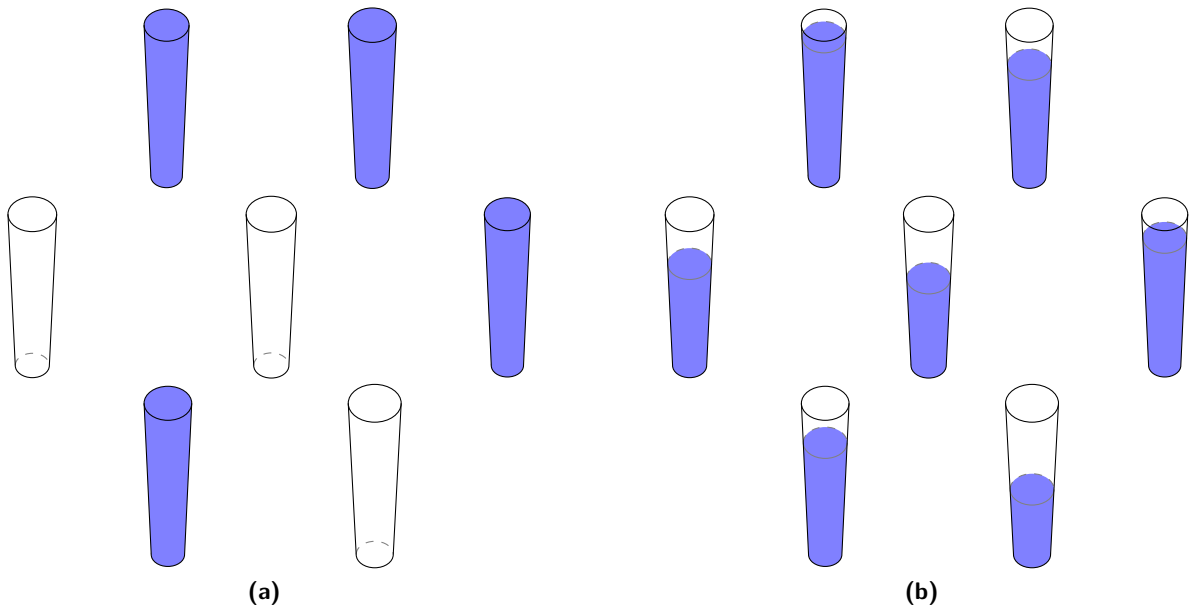


Figure 5.3 Disorder between neighboring pores during absorption (a) and desorption (b). Important is the larger degree of disorder upon the absorption process. Upon condensation pores fill immediately when the spinodal pressure $P_{\text{sp}}(d_{\min})$ is reached, where d_{\min} is the radius of the opening at the small end. The evaporation is continuous at equilibrium pressure $P_{\text{eq}}(d)$ and empties each pore simultaneously while the diameter d is large enough.

(open pores) where this is the case. A possible interpretation is the degree of disorder caused inside the membrane by the respective process. As the membrane contains pores open on both ends, the condensation takes place at spinodal pressure $P_{\text{sp}}(d_{\text{pore}})$. Due to the distribution of pore sizes, funnelization, corrugation and constrictions, the pores fill at different pressures $P_{\text{sp}}^1 \neq P_{\text{sp}}^2$. At a given pressure

$$P_{\text{sp}}^1 < P < P_{\text{sp}}^2,$$

where P_{sp}^1 shall correspond to the smallest pore diameter found on the membrane and P_{sp}^2 the largest one, the state of the membrane regarding filled and empty pores is assumed to be comparable to figure fig. 5.3(a). The hexane evaporates at equilibrium pressure P_{eq} , though. That means that, assuming the same pore size distribution, funnelization, corrugation and constrictions, the pores empty continuously. The theoretical state of the membrane is visualized in fig. 5.3(b).

The difference is that during the condensation process neighboring pores can be in very different states meaning empty and filled, while for evaporation the pores only show different levels of liquid during most of the process. As a result, the absorption of hexane creates a higher grade of disorder than the desorption and therefore causes a more significant drop of the transmission coefficient (compare fig. 5.4(a)).

The occurrence of the small peak in between two dips of the evaporation transmission cannot be explained by this theory. Moreover, the later analysed membranes of wafer 295 and 296 yield a more even dip distribution (compare fig. 5.4(c) and fig. 5.4(b)) and upon reducing the pore diameter of 295 using ALD, the membranes even show the inverse behaviour (fig. 5.4(d)).

The first phenomenon could be explained by the pores being less flawed talking corrugations and funneling. The latter assumption is backed by the fact, that the transmission drops of 295d are of smaller magnitude than those of 296b. While both are open pore membranes, membrane 295d is only half as thick as 296b, meaning the pores are only half as long and therefore the influence of the funneling aspect is reduced respectively by half.

The second one remains unclear though.

5.2 Analysis of wafer 292

Of wafer 292, the membranes 292c and 292d have been measured. The pores were opened by floating as explained in section 4.1.1.3. The thickness of the membranes is

$$l_{\text{pore}} = 60 \mu\text{m}. \quad (5.13)$$

Expected is an absorption and desorption isotherm with a hysteresis as explained in section 3.6.2.2. While by theory, the condensation branch is supposed to be steeper than the evaporation branch, the measurements show the opposite. The condensation seems to have a tail to lower pressures. This can be explained by inhomogeneous pore openings. In fact, the membrane's pores were not well opened after the first barrier layer dissolution process (compare section 4.1.1.3), as determined from MEB views, and has therefore been opened using a second floating process. That might have caused an increase of the funneling and/or corrugations and also left some bad open pores.

5.3 Analysis of wafer 296

As already mentioned in section 4.1.1.3, the *barrier layer* dissolution shall be taken a closer look at. The reason for this is explained in the following. Therefore, some analysis of wafer 295, which has not yet been introduced, needs to be done at this place. The more detailed analysis of wafer 295 will be done in section 5.4, though.

Following, the pore opening of membrane 295 c shall be inspected:

After t_1^{295c} of floating on phosphoric acid, white speckles appear on the wafer. As this phenomenon looks similar to the observation made during the absorption process of an isotherm, this can be interpreted as the membrane filling with the acid. Due to the capillary flow rate of phosphoric acid in pores of diameter $d_{\text{pore}}^{295c} = 40 \text{ nm}$, a single pore fills within $t_{\text{fill}}^{295c} = 5 \text{ s}$??? quote physical basics ????. That the milky aspects occur over about $\Delta t^{295c} = 3 \text{ min}$ implies that some pores fill minutes before others. Therefore, the pore size distribution is increased during this time. The caused distribution in radius can be approximated by the etch rate of the acid.

The barrier layer's thickness of wafer 295 is about $d_{\text{barrierlayer}}^{295c} = 30 \text{ nm}$ as observed on the MEB views shown in fig. 5.5(a). As the first milky speckles appear after $t_1^{295c} = 20 \text{ min}$, the etch rate is about

$$e = 1,5 \frac{\text{nm}}{\text{min}}. \quad (5.14)$$

This yields a diameter distribution of

$$\Delta d_1^{295c} = 9 \text{ nm} \quad (5.15)$$

which is only due to the opening process of the pores. Furthermore, the wafers are left floating until the whole upper side is observably covered by a liquid film (compare figure???). This state has been reached after $t_2^{295c} = 40 \text{ min}$ of floating. Thus, by the theory explained above, the pores should widen by up to

$$\Delta d_2^{295c} = 60 \text{ nm}. \quad (5.16)$$

Summing up the section above, the pore diameters should be distributed around

$$d_{\text{pore}}^{\text{295c-theory}} = 109 \text{ nm}. \quad (5.17)$$

The analysis of the MEB vues of the membrane yield a diameter distribution around

$$d_{\text{pore}}^{\text{295c-MEB}} = 58 \text{ nm}, \quad (5.18)$$

though. Thus, at some point there must be a mistake in the interpretation of the observations.

The idea behind the following experiments with wafer 296 is to better understand what happens during the *barrier layer* dissolution process and to find a systematic way to open the pores with a minimal pore diameter increment and diameter distribution increment. Floating and immersing single membranes in phosphoric acid shall lead to a calibration of the respecting etch rates $e_{\parallel \text{pores}}$ and $e_{\perp \text{pores}}$.

The thickness of wafer 296 is

$$l_{\text{pore}}^{296} = 60 \mu\text{m}. \quad (5.19)$$

As explained before in section 4.1.1.3, this wafer shall be used to further understand the barrier layer dissolution. The goal is to be able to produce the membranes in a more controlled way an to hereby reduce the funneling aspect of the pores. fig. 5.6 shows the treatments of the membranes and gives an overview over the conducted measurements. While the membranes 296c and 296d are immersed in phosphoric acid for

$$\begin{aligned} t_{\text{im}}^{296c} &= 6,5 \text{ min}, \\ t_{\text{im}}^{296d} &= 13 \text{ min}, \end{aligned} \quad (5.20)$$

296e and 296f are only floated on the acid on the barrier layer side for

$$\begin{aligned} t_{\text{fl}}^{296e} &= 13 \text{ min}, \\ t_{\text{fl}}^{296f} &= 26 \text{ min} \end{aligned} \quad (5.21)$$

respectively. Assuming the etch rate to be equal for both sides of the barrier layer, meaning from within the pore and from the outside, the thickness of the barrier layer of 296c and 296e and also of 296d and 296f should be equal after the dissolution. Moreover, all pores should still be closed assuming an etch rate of approximately $1 \frac{\text{nm}}{\text{min}}$. The latter should be clearly visible on the volumetric measurements. Furthermore, only the pores of the immersed membranes are expected to be widened. The horizontal etch rate, which according to section 4.1.1.3 must be different from the one attacking the barrier layer vertically, shall be put a figure to in the run of the evaluations.

Section 5.3.1 shows a full comparison of the volumetric measurements of the membranes mentioned above. Additionally, membrane 296a (closed pores) and 296b before and after the barrier layer dissolution are presented on the graph. So the membranes 296a and 296b cp serve as reference for closed pore membranes, while 296b op serves for open pore membranes. The comparison of the different membranes implies that indeed, all pores are still closed for the four treated membranes as the shapes of their isotherms match the one of 295a and 296b cp while they do not match the one of 296b op. Moreover, no big diameter variation can be observed. Which cannot be observed though, that is weather the pores already have microscopic openings on the barrier layer side. If that were the case, hexane would condense there at spinodal pressures lower than the equilibrium pressure of the small ends. Hereby, the pores would be left in a closed shape. This case would not be visible on the volumetric measurements as the condensed amount of hexane necessary to close the pores were so small. If the openings were so large already as for the spinodal pressure to be larger than the equilibrium pressure of the small end, that case would be visible on the isotherm because whole pores would fill at higher pressures. Therefore, the latter case can be excluded.

Next, the floated and immersed membranes shall be regarded separately.

5.3.1 Floated membranes 296e and 296f

The comparison of the volumetric measurements of the membranes 296e, 296f and for the reference of an untreated membrane 296a are shown in section 5.3.1. Even though the wafer has been produced as a whole and the membranes 296e and 296f have only been floated on ??? acid without opening the pores, by theory leaving the pore diameters unchanged, a clear offset in diameter between 296a and the other two membranes is visible. As 296e and 296f are pretty superimposed though and also the shapes of isotherms match according to section 5.3, no error in the before made interpretations

Table 5.1 Diameter reduction per minute of immersion derived from the isotherms of the membranes 296a, 296c, 296d.

| $t_{\text{im}}[\text{min}]$ | $\Delta d_{h=60 \mu\text{m}}[\text{nm}]$ | $\Delta d_{h=0 \mu\text{m}}[\text{nm}]$ |
|-----------------------------|--|---|
| 0 | 0 | 0 |
| 6,5 | 3 | 0 |
| 13 | 6 | 0 |

of the pores still being closed can be implied. This leaves only the possibility of the pore diameters being distributed throughout the wafer and hereby throughout the membranes.

As a reminder, all the pores are closed. Regarding the light transmission measurement, the transmission dips of condensation and evaporation are expected to be of the same magnitude as both processes occur at equilibrium pressure. Unlike theory, section 5.3.1 shows deeper transmission minima for the condensation than it does for the evaporation. This cannot be explained by the theory explained in section 5.1.3.1. One possible approach could be the corrugations within the single pores that lead to an irreversible absorption and desorption isotherm.

5.3.2 Immersed membranes 296c and 296d

Figure 5.9(a) compares the volumetric and also the transmission measurements of the immersed membranes 296c and 296d, again adding the untreated membrane 296a. As explained in section 3.6.1.2, condensation and evaporation in a closed funnelled pore occur at equilibrium pressure. Pores that are open on the large end start filling from the bottom and evaporating from the top so, regarding the isotherms in fig. 5.9(a), the lower end of the isotherm rising represents the small bottom end of the pores. This lower end of all three isotherms seems to be superimposed while the top end, representing the large open end of the pores, moves to larger diameters for longer immersion times. As the effect seems to occur linearly over the whole length of the pores, the acid seems to be saturating within the pores losing etching power. By section 3.6.1.2, the process can be visually interpreted as a pore straightening as shown in fig. 5.10(b). Moreover, the increase of the funnelling aspect seems to be linear at least within the first 13 minutes of the immersion as doubling the immersion time yields double the diameter shift on the volumetric isotherm (compare eq. (5.20)). For instance, table 5.1 shows the diameter increase of the pores due to the immersion of the membranes in phosphoric acid. Using this data along with the assumption of a linear etch rate gradient along the length of the pore, the respective etch rate can be plotted as shown in fig. 5.10(a). Here, the parameter h is used as the height within a vertical pore, where $h = 60 \mu\text{m}$ refers to the open top end of a $60 \mu\text{m}$ long pore that is closed on the bottom side.

As for the transmission isotherms, the shifts of the beginning of the condensation dip and also the end of the evaporation dips correspond to the interpretation explained above. On the other hand, the magnitude difference of the three isotherms' dips cannot be explained, neither interpreted at this point.

5.4 Analysis of wafer 295

Wafer 295 is only

$$l_{\text{pore}}^{295} = 30 \mu\text{m} \quad (5.22)$$

thick. Hereby, the effect of the funneling observed upon the previously measured membranes of a thickness of

$$l_{\text{pore}}^{292,293,294,296} = 60 \mu\text{m} \quad (5.23)$$

is expected to be reduced. Assuming that the funneling aspect is linear implies a reduction of the effect by half. Finally, the membranes' pore diameters are reduced using ALD. Figure 5.11 shows the treatments and measurements of the inspected membranes of wafer 295.

5.4.1 Membrane 295a

To start with, membrane 295a shall be analysed. It is untreated, meaning that the pores are still closed on one end by the barrier layer. Expected are straight pores of a diameter of approximately 40 nm diameter with a significantly reduced funneling aspect resulting in a rather upright evaporation isotherm. The result is displayed in fig. 5.12. The absorption and desorption isotherm shows a kink at two thirds of the height, which cannot easily be explained. While for straight pores, a straight isotherm rising is expected, the observed kink could speak for a deformation as shown in fig. 5.13, assuming that it is due to intra pore defects, not inter pore defects. Regarding inter pore defects, a discreet pore diameter variation could cause this shape of isotherm. Again, the reason for such a discreet distribution in pore sizes is not clear.

5.4.1.1 Membrane 295a - after aluminum dissolution bath

Membrane 295a is measured again after a bath in the acid used for the aluminum dissolution as explained in section 4.1.1.2. The point of this is to see, if the wafers immersion in the acid when dissolution the remaining aluminum after the anodizing might cause any unexpected defects or pore widening already. As the anodizing of wafer 295 has been conducted with the same parameters as the other wafers before (for instance wafer 296, the pore diameters are expected to be approximately the same. Referring to wafer 296 the pore diameters of

$$d_{\text{pore}}^{296a} = 45(5) \text{ nm}$$

do not fit the ones results of membrane 295a with???

$$d_{\text{pore}}^{295a} = 55(6) \text{ nm}.$$

Finally, the probing of the aluminum dissolution process, which by theory is not supposed to attack the alumina of the membranes and therefore has not been taken a deeper look at, yields the before and after result displayed in section 5.4.1.1. In between the two measurements, the membrane has been immersed for

$$t_{\text{immerse}} = 4.5 \text{ h}$$

in ??? acid at a temperature of

$$T_{\text{acid}} = 0^\circ\text{C}.$$

The aluminum dissolution of the wafers takes approximately

$$t_{\text{Aldiss.}} = 4 \text{ h} \quad (5.24)$$

and uses the same parameters which makes for a relevant approximation of what changes to the pores are expected during the before mentioned production step. The change to the pore diameters is

$$\Delta d_{\text{pore}}^{\text{Aldiss.}} = 3 \text{ nm}. \quad (5.25)$$

Both, the starting points of the condensation rise and of the evaporation drop are shifted in the same way. Moreover, the hysteresis did not increase during the process. These two observations speak for the pore widening being homogeneous and also the corrugations not having increased during the etching. Therefore, the production step of the aluminum dissolution conducted as explained in section 4.1.1.2 can be disregarded as a cause of big pore impurities.

5.4.2 Membrane 295d, 295e, 295f, 295g

The membranes 295d, 295e, 295f, 295g yield very upright isotherms without any kinks or transmission defects. On the contrary, the membranes 295e and 295f superimpose perfectly, while 295d and 295g are only shifted to larger diameters ??. For all the membranes, the transmission dips of absorption and desorption show the same value. This can only be explained by almost perfectly straight pores if the disorder theory in section 5.1.3.1 are assumed to be correct. Also, regarding the conversion to pore diameters according to KELVIN equation (compare section 3.5, the funneling aspect is the weakest so far measured in this experiment. This can be explained by the inverse of the effect observed upon the opening experiments of wafer 296 ??.

5.4.2.1 Membrane 295g

Finally, membrane 295g shall be assumed to be good enough in the sense of pore size distributions, funnelling and corrugations as to be used to check on the theories of condensation and evaporation in confinement. From the untreated MEB images, the difference of pore sizes on the aluminum and solution side, which are due to the funnelling aspect of the pores, can be approximated. To this end, the values

$$\begin{aligned} d_{\text{pore}}^{\text{Sol}} &= 67 \text{ nm} \\ d_{\text{pore}}^{\text{Al}} &= 60 \text{ nm}. \end{aligned} \tag{5.26}$$

Moreover, the funnelling is assumed to be linear in the following. Therefore, the threshold, that needs to be set for the distribution analysis for solution and aluminum side respectively, can be adapted using some basic geometry:

5.4.3 Membrane 295c

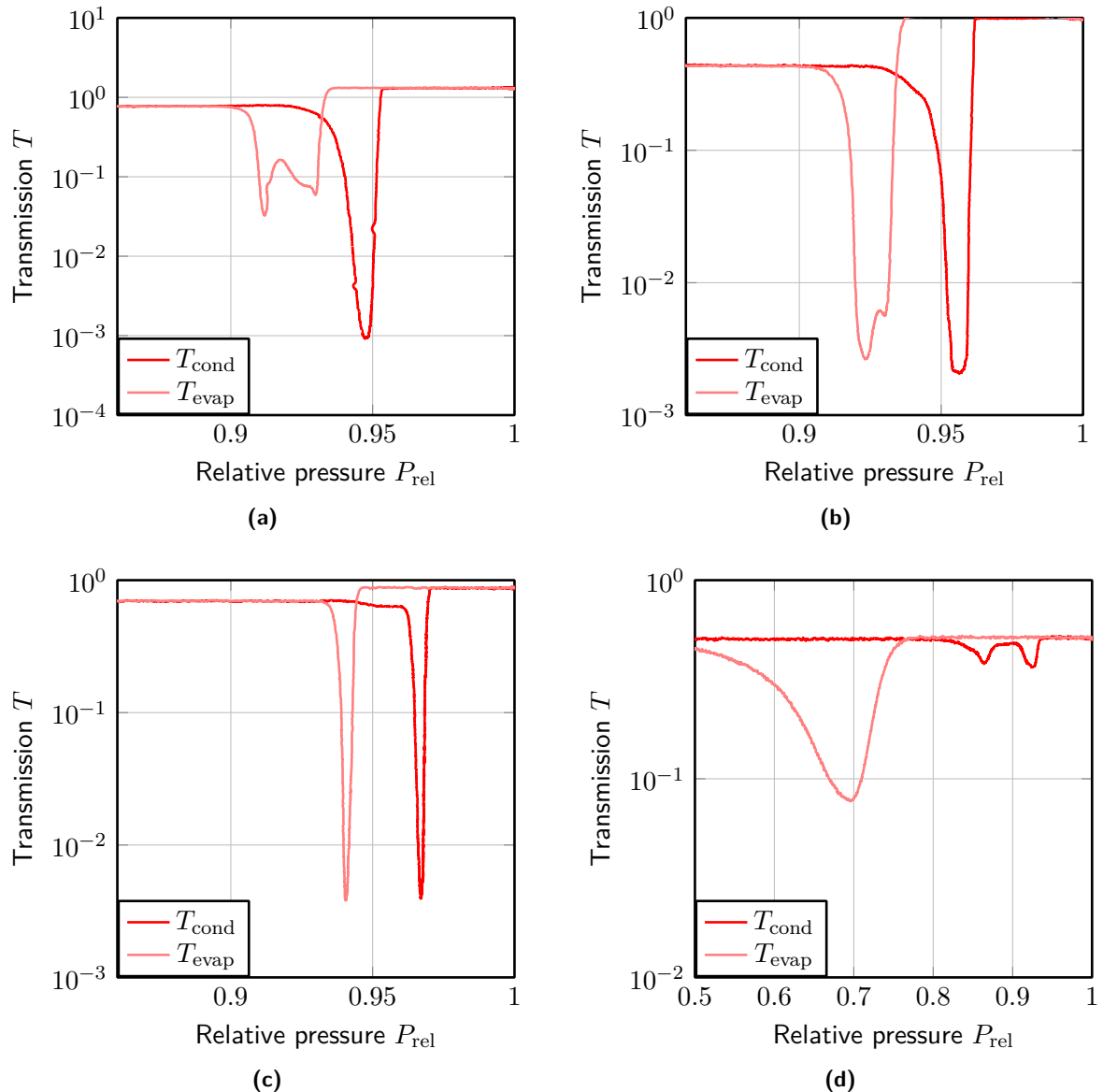


Figure 5.4 P_{rel} transmission isotherms of the membranes 292d (a), 296b (b), 295d (c), and 295f 200ALD (d). All membranes have open pores. Unlike the isotherm of membrane 292d, the transmission drops of condensation and evaporation are of the same magnitude. The magnitudes of condensation and evaporation dip are reversed in respect to membrane 292d for membrane 295f 200ALD.

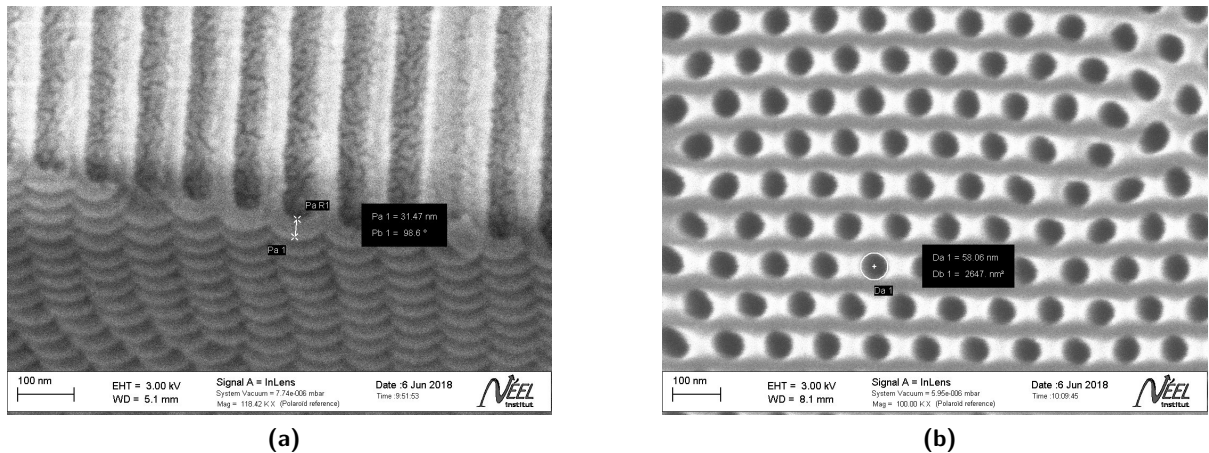


Figure 5.5 MEB views of membrane 295c. The thickness of the *barrier layer* is measured directly with the ZEISS software in (a). As the membrane is not oriented exactly orthogonal to the microscope and the perspective of the layer is a bit distorted, the value can only be used as a rough approximation. (b) shows the pores on the solution side of the membrane.

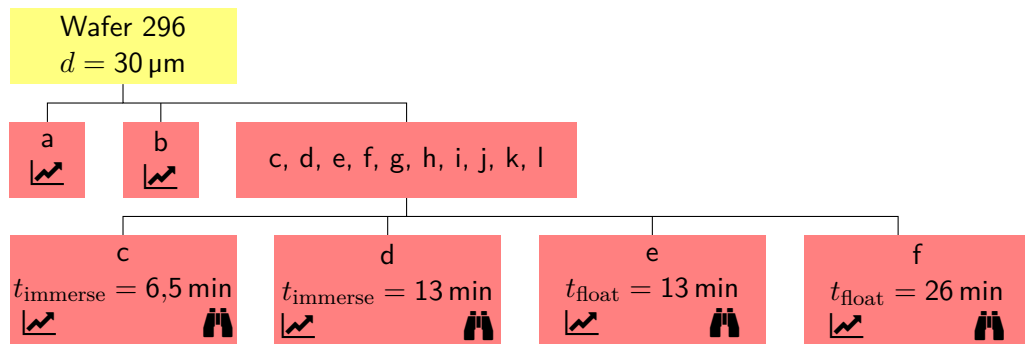


Figure 5.6 Wafer 296 processing scheme. While a signifies a recorded isotherm, the means MEB pictures have been taken. Red marks pores closed on one end, green pores open on both ends. The processed wafers are immersed in phosphoric acid for t_{immerse} or floated on for t_{float} .

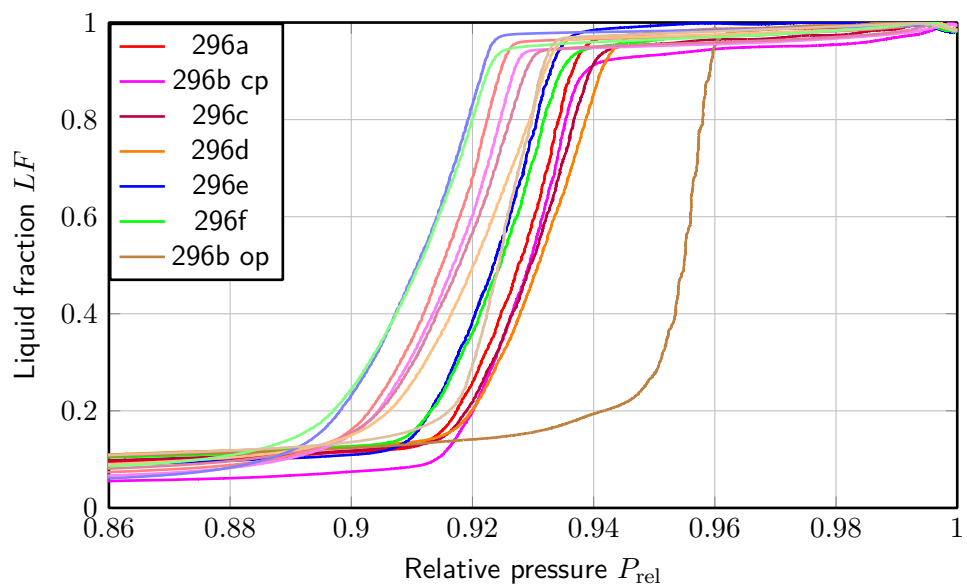


Figure 5.7

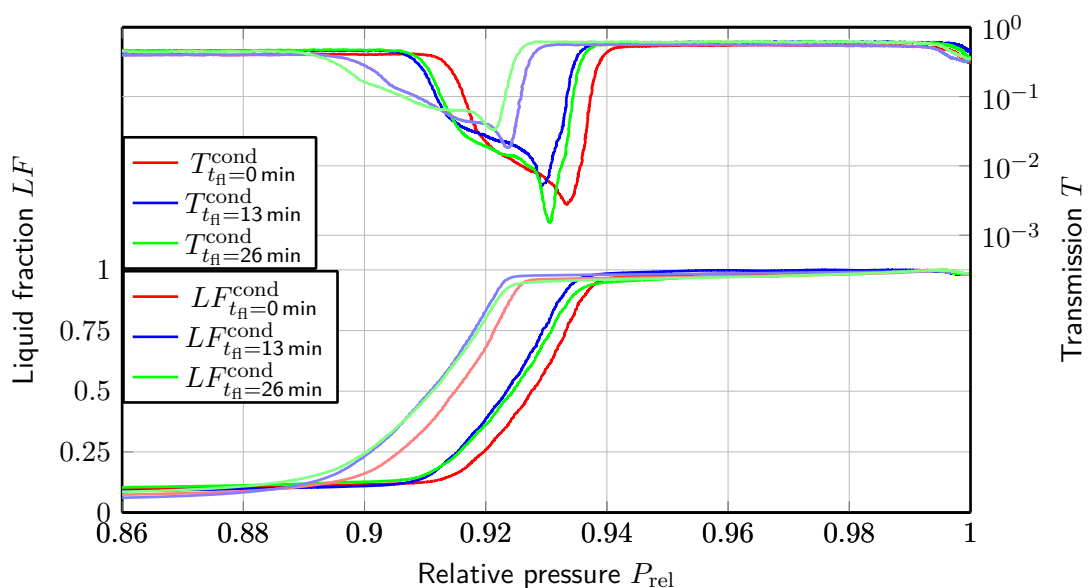


Figure 5.8 Comparison of the isotherms measured for the membranes 296a, 296e and 296f. While the pore diameters are marginally smaller for the membranes 296e and 296f than they are for 296a, the overall picture is equivalent. It makes for closed pores with the same funnelling aspect.

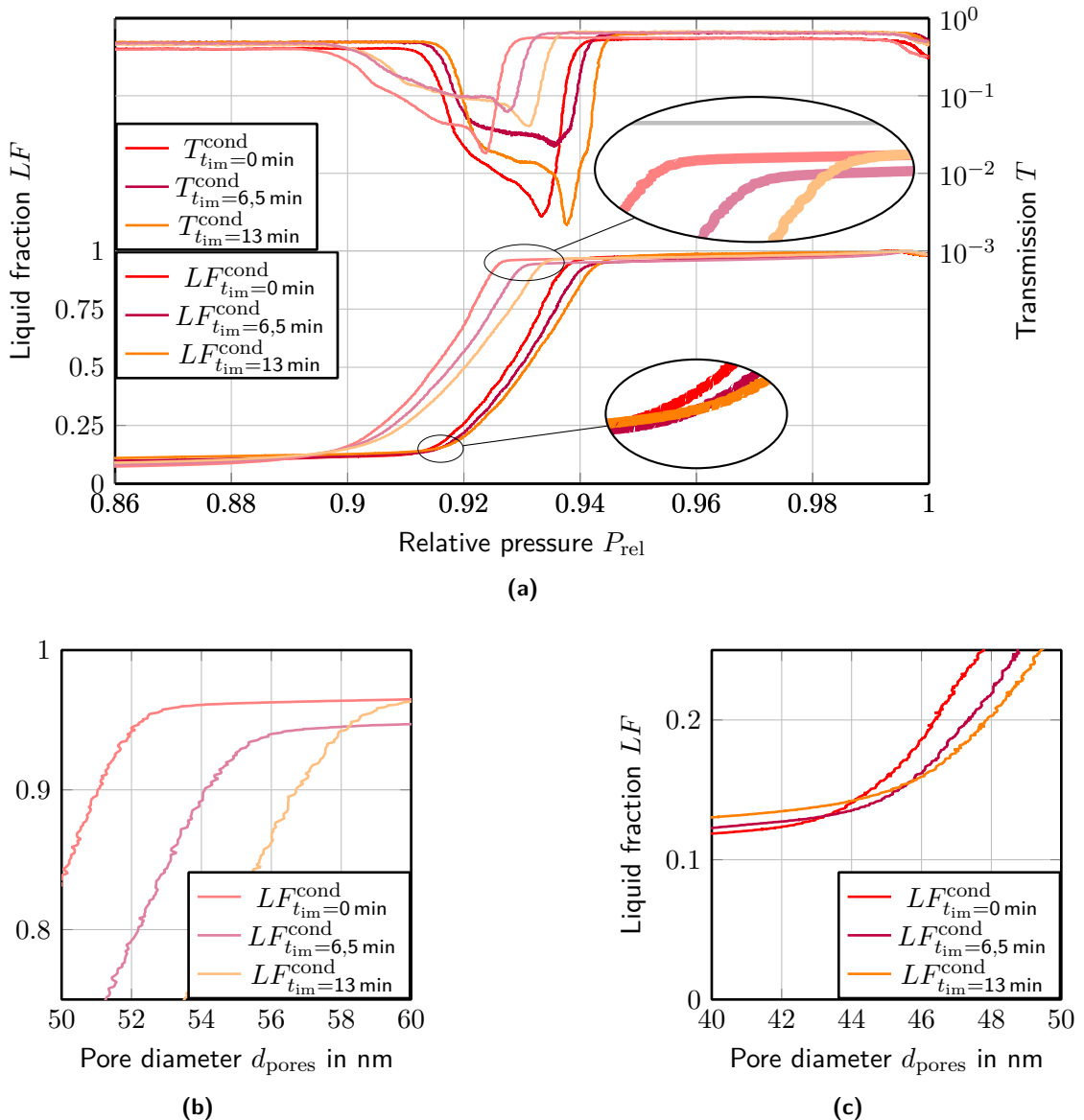


Figure 5.9 (a) shows the isotherms of the immersion experiment conducted using wafer 296. The shift to larger pressures of the beginning of the evaporation branch and the unmoving beginning of the condensation branch are clearly visible. (b) and (c) are higher resolution plots of the relevant areas of the evaporation and respectively condensation branch of the isotherm on a pore diameter scale. For interpretations please refer to section 5.3.2. ???EXPLAIN WHY EVAP START AND COND START ARE THE SPOTS TO LOOK AT ???

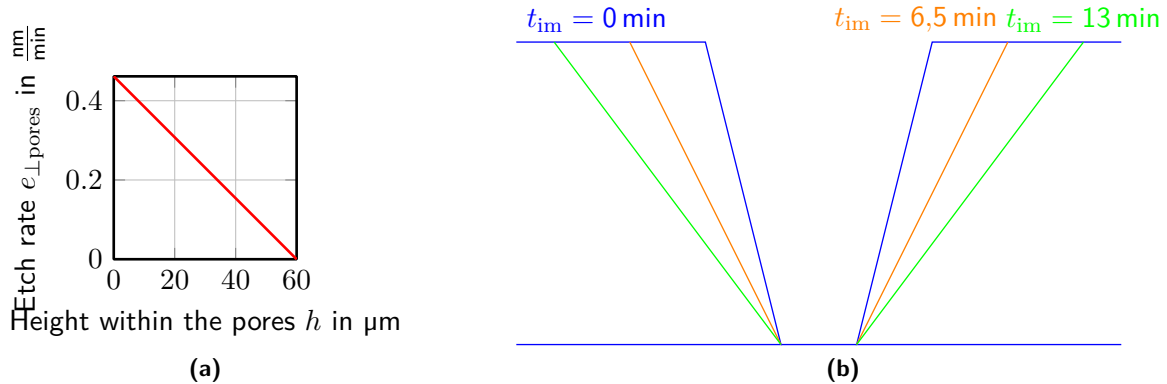


Figure 5.10 Immersion of a closed pore membrane resulting in an increase of the funnelling aspect of the pores as shown in (b) due to the saturation of the acid within the pores. The visualized theory is backed by the isotherms in fig. 5.9(a) which lead to the etch rate dependency plotted in (a) on the height within a pore. For further explanations please refer to section 5.3.2.

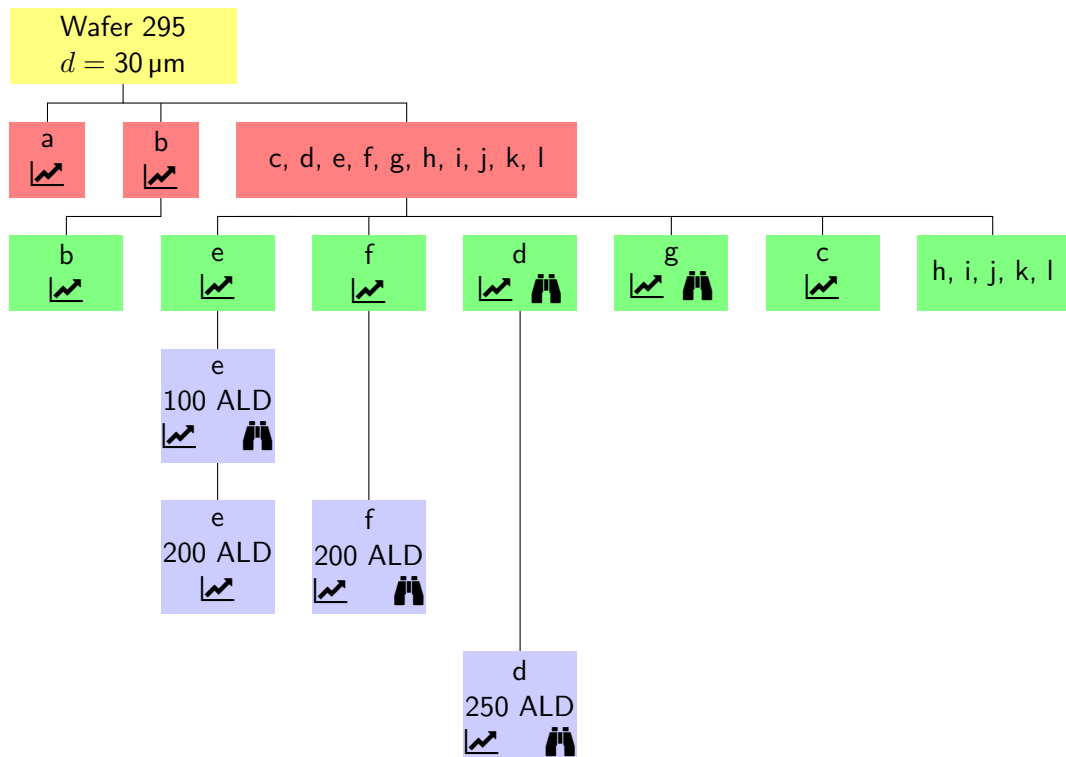


Figure 5.11 Wafer 295 processing scheme. While a signifies a recorded isotherm, the means MEB pictures have been taken. Red marks pores closed on one end, green pores open on both ends. The blue marked membranes have undergone n cycles of ALD depositing.

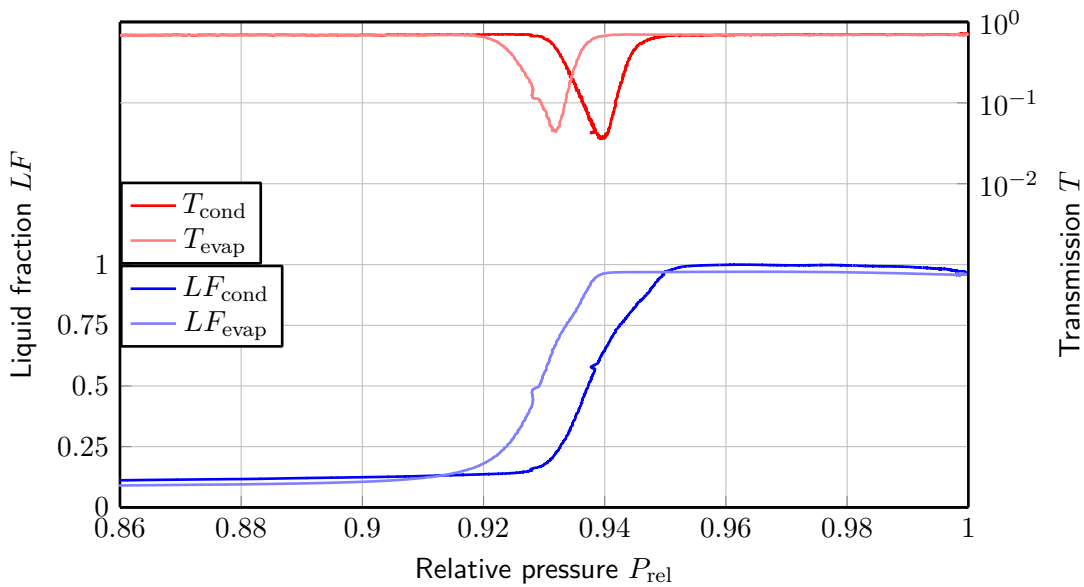


Figure 5.12

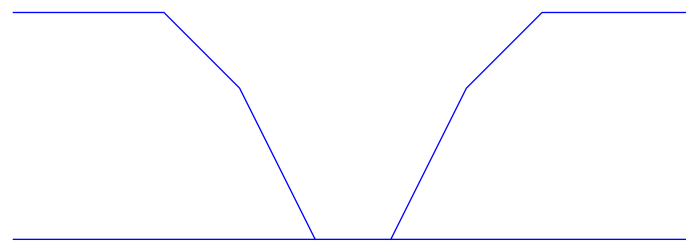


Figure 5.13 Possible shape interpretation of the volumetric isotherms of membrane 295a for a single pore. If the interpretation were correct, an incontinuity ?? of the anodizing current could be the reason for the change in funnelling.

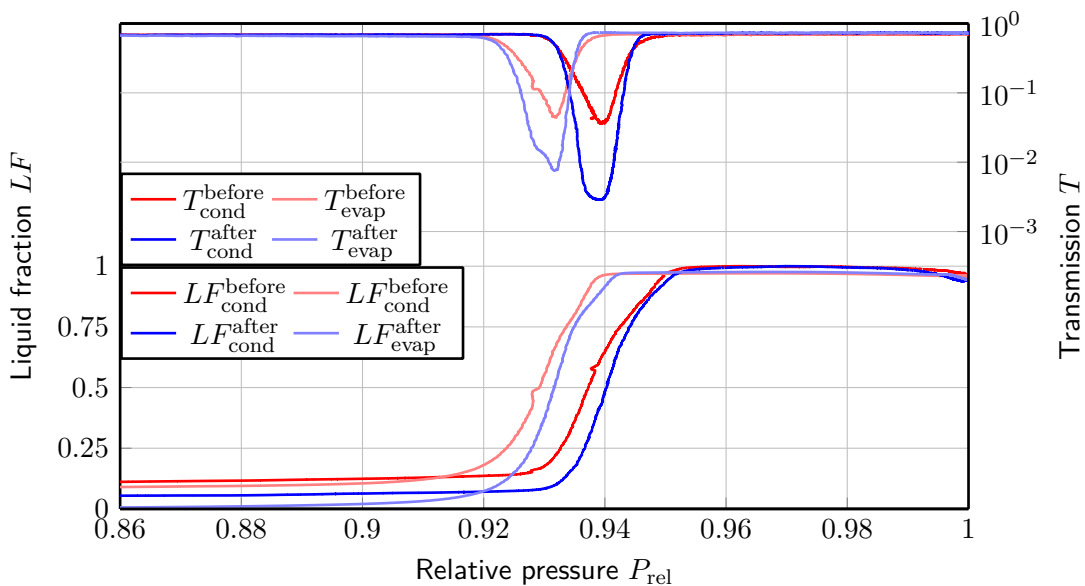


Figure 5.14 Comparison of the isotherms of membrane 295a (closed pores) before and after a 4,5 h bath in aluminum dissolving acid (compare section 4.1.1.2). A small but homogenous shift of the isotherm to higher pressures is clearly visible. This implies that the acid does not only attack aluminum but also alumina.

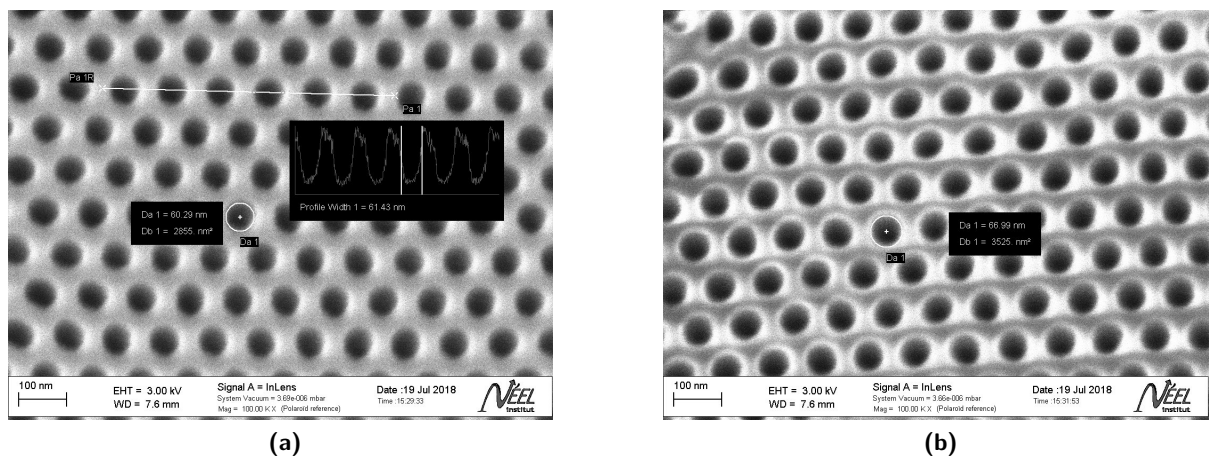


Figure 5.15 MEB images of membrane 295g of aluminum (a) and solution side (a). The measurements of the pore diameters were done immediately using the ZEISS software of the microscope.

Bibliography

[Cd15] Universität Konstanz: Corporate Design Manual. Universität Konstanz, (2015)